Experimental investigation of m~~M~~ini Gurney f~~F~~laps in combination with vortex generators for improved wind turbine blade performance

Jörg Alber[1], Marinos Manolesos[2], Guido Weinzierl-Dlugosch[3], Johannes Fischer[3], Alexander Schönmeier[1], Christian Navid Nayeri[1], Christian Oliver Paschereit[1], Joachim Twele[4], Jens Fortmann[4], Pier Francesco Melani[5], Alessandro Bianchini[5].

[1] Technische Universität Berlin, Hermann-Föttinger Institut, Müller-Breslau-Str. 8, 10623 Berlin, Germany
[2] College of Engineering, Swansea University, Bay Campus, Fabian Way, Swansea, SA1 8EN, United Kingdom
[3] SMART BLADE GmbH ®, Waldemarstr. 39, 10999 Berlin, Germany
[4] Hochschule für Technik und Wirtschaft Berlin, Wilhelminenhofstraße 75A, 12459 Berlin, Germany
[5] Università degli Studi di Firenze, Department of Industrial Engineering (DIEF), Via di Santa Marta 3, 50139 Firenze, Italy

Correspondence to: Jörg Alber (joerg.alber@posteo.de)

Abstract

This wind tunnel study investigates the aerodynamic effects of Mini Gurney flaps (MGFs) and their combination with vortex generators (VGs) on the performance of airfoils and wind turbine rotor blades. VGs are installed on the suction side aiming at stall delay and increased maximum lift. MGFs are thin angle profiles that are attached at the trailing edge in order to increase lift at pre-stall operation. The implementation of both these passive flow control devices is accompanied by a certain drag penalty. The wind tunnel tests are conducted at the Hermann- Föttinger Institut of the Technische Universität Berlin based on two airfoils that are characteristic for different sections of large rotor blades. ~~-~~ Lift and drag are determined using a force balance and a wake rake, respectively~~Lift is determined with a force balance and drag with a wake rake~~, for static angles of attack ~~from~~ between -5° to 17° at a ~~constant~~ Reynolds number of 1.5 million. The impact of different MGF heights including 0.25%, 0.5% and 1.0 % and a~~n uniform~~ VG height of 1.1 % of the chord length ~~are~~ is tested and evaluated ~~on three airfoils that are characteristic for different sections of large rotor blades~~. Furthermore, the clean and the tripped baseline cases are considered. In the latter, leading edge transition is forced ~~by means of~~ with Zig Zag (ZZ) turbulator tape. The preferred configurations are the smallest MGF on the NACA63(3)618 ~~and the AH93W174 (mid to tip blade region)~~ and the medium sized MGF combined with VGs on the DU97W300 ~~(root to mid region)~~. Next, the experimental lift and drag polar data is imported into the software QBlade in order to design a generic rotor blade. The blade performance is simulated with and without the add-ons by means of ~~based on~~ two case studies. In the first case, the retrofit application on an existing blade mitigates the adverse effects of the ZZ tape. Stall is delayed and the aerodynamic efficiency is partly recovered leading to an improvement of the power curve. In the second case, the new design application allows for the design of a more slender blade while maintaining the rotor power ~~output~~. ~~Moreover,~~ ~~T~~ ~~t~~his is alternative ~~e alternative~~ blade appears to be more resistant against the adverse effects of forced leading edge transition.

Formatted: Font: 16 pt
Formatted: Font: 16 pt
Formatted: German (Germany)
Formatted: English (United States)
Formatted: English (United States)
Formatted: English (United States)
Formatted: English (United States)
Commented [D1]: RC2: Airfoil is removed for space economy

1. Introduction

1.1 General outline

The ~~study~~ is report is divided into the following sections.

Introduction. The concepts, mechanisms and applications of Gurney flaps (GFs), ZZ tape and VGs are introduced. The literature review is focused on very small GF heights, so-called MGFs, and their combination ~~of GFs~~ with VGs.

Airfoil simulations. The simulation software XFOIL (Drela, 1989) is used to determine the appropriate ~~dimensions~~ size of each passive flow control (PFC) device in relation to the local boundary layer thickness of ~~the following airfoils:~~ the NACA63(3)618~~, the AH93W174~~ (tip region) and the DU97W300 (root region).

Experimental set-up. The wind tunnel test section, the measurement methods and the data reduction process are specified including the force balance for the lift, and the wake rake for the drag measurements at a constant Reynolds number of $Re = 1.5 \cdot 10^6$.

Experimental results. The ~~baseline~~ lift and drag polars, c_l (α) and c_d (α), ~~of each airfoil~~ are ~~validated against literature data~~presented. Different combinations of MGFs and VGs are ~~assessed~~ evaluated according to characteristic parameters, i.e. the lift performance, the stall behavior and the aerodynamic efficiency.

Rotor blade performance. The experimental data ~~of the preferred configurations~~ is imported into the software QBlade (Marten, 2020) in order to create a generic rotor blade. The blade performance is simulated ~~based on~~by means of two case studies, the retrofit application on an existing, and the new design application on ~~an alternative~~ an alternative rotor blade.

1.2 Gurney flaps

This aerodynamic device is named after the US racecar driver Dan Gurney. In the early 1970s, he applied it to the rear spoilers achieving significant improvements in the downforce and thus the traction of his Formula One vehicles, see Liebeck (1978). Passive GFs are categorized as static miniflaps or miniature trailing edge devices (MiniTEDs), as described by González-Salcedo et al. (2020). ~~Hence, they~~ They are different to the concept of flexible trailing edge (TE) flaps that are integrated into the very TE section, see Barlas and van Kuik (2010). The first reference to miniflaps dates back to the early 20th century and was probably developed by Gruschwitz and Schrenk (1933). Zaparka (1935) registered the first patent on active miniflaps for use on airplane wings. Various patents of passive miniflaps followed, particularly in aviation. Boyd (1984) and later Brink (2002) claimed the rights on different versions of wedge-shaped TE flaps. Henne and Gregg (1989) patented the shape of a diverging trailing edge (DTE) of a transonic airfoil generating similar aerodynamic effects than the GF. Bechert et al. (2001) registered a patent on so-called three dimensional (3D) GFs, i.e. profiles with slits, serrations, holes, as well as tiny vortex generators attached to the miniflap itself ~~in order~~ to stabilize the ~~otherwise~~ unsteady wake field. Wang et al. (2008) published a comprehensive review of GFs for use on rotor blades of helicopters and wind turbines. In contrast to the large amount of patents and publications, there are only few examples of standardized or commercialized GF applications on rotor blades of horizontal axis wind turbines (HAWTs). For instance, Vestas (2019) offers GFs in combination with VGs as aerodynamic

Commented [D2]: RC1(Q3minor): PFC not defined

Commented [D3]: RC2: AH93W174 was removed for space economy

Commented [D4]: RC2: typo

upgrades of operating wind turbines predicting the average energy production (AEP) to increase by 1.7%. Another example is the blade design of the 10 MW reference wind turbine of the Danish Technical University (DTU) with a total rotor radius of R = 89.2 m. The inner blade part alongside the local rotor radius of 5%R < r < 40%R was equipped with wedge-shaped GFs including heights of 3.5%, 2.5% and 1.3%, respectively, in relation to the local chord length, c. Bak et al. (2013) claim significant aerodynamic performance improvements, especially on relatively thick airfoils with a maximum thickness ~~of $h_{th,max}$ ≥~~greater than 30%c.

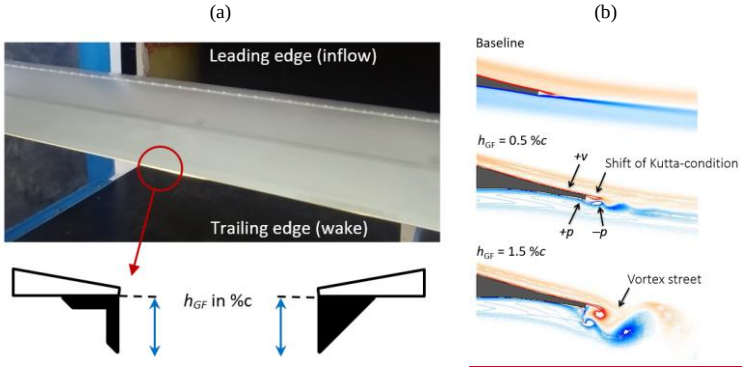

Figure 1. (a) NACA63(3)618 during wind tunnel tests. Vortex generator array and Gurney flap. Definition of Gurney flap height of rectangular and triangular profiles in side view. (b) CFD simulations of the HQ17. Wake structures at α = 0.~~0~~° and Re = 1·10^6 for different Gurney flap heights, reproduced and modified from Schatz et al. (2004a).

Figure 1a displays the typical GF shapes~~s~~, i.e. the rectangular, or L-shaped, and the triangular, or wedge-shaped, profiles. Typically, ~~T~~they are ~~attached~~ installed at the TE and normal to the pressure side of wings and rotor blades~~, normal to the pressure side~~. In both cases, the effective GF height, h_{GF}, is expressed in ~~in percentage of the chord length, %~~c, without taking the original TE thickness~~, h_{TE},~~ into account. For identical h_{GF}, the aerodynamic effect of both ~~GF~~ GF profiles is considered to be very similar, as discussed in Appendix B2. It is noted that GFs are also used at a certain distance away from the TE. These mini tabs, see Bach et al. (2014), are out of the scope of this study. ~~Sect 4.1.2~~.

Figure 1b illustrates the principal changes of the flow field for two different GF heights, as first reported by Liebeck (1978). Adjacent to the TE modification, a highly efficient vortex system is formed consisting of one vortex upstream and two counter rotating vortices immediately downstream. Bechert et al. (2000) and Schatz et al. (2004b) showed by means of experimental and numerical investigations that the wake ~~flow~~ structures are quasi two dimensional (2D) at pre stall operation. The recirculation region changes the Kutta condition, so that the rear stagnation point is shifted downstream and deflected downwards, see also Jeffrey et al. (2000) and Cole et al. (2013). The modifications of the flow field lead to the following set of simultaneous effects.~~:~~

Formatted: Left

Formatted: Pattern: Clear

Formatted: Pattern: Clear

Commented [D5]: RC1 (Q5major): different chordwise positions of GFs were mentioned

Formatted: Pattern: Clear (Yellow)

- Lift performance.~~:~~ The suction peak is higher and coupled with a positive pressure built-up right in front of the GF, as such increasing the pressure difference between the suction ~~side (SuS)~~ and the pressure side ~~(PS)~~. As a results, the effective camber is enhanced, ~~thus shifting the lift curve upwards~~ so that the same lift coefficient, c_l ~~(α)~~, is already reached at a lower angle of attack (AoA), α. Furthermore, the adverse pressure gradient on the ~~SuS~~ suction side becomes milder generating a higher maximum lift coefficient~~s~~, $c_{l_{max}}$ ~~, as stall is initiated.~~
- Drag behavior.~~:~~ The recirculation or low pressure region in the immediate wake ~~causes~~ leads to an increased momentum loss and thus higher drag coefficient~~s~~, $c_d(\alpha)$. In addition, the intensity of the wake unsteadiness is stronger, especially if vortex shedding is initiated in the form of an absolute instability, as illustrated ~~in Figure 1b~~ for h_{GF} = 1.5%c in Figure 1b.

Field Code Changed

Field Code Changed

1.3 Zig Zag tape

ZZ turbulator tape is implemented to initiate the boundary layer (BL) transition at a fixed chord position, see Figure 3a. Its height, h_{ZZ}, should be ~~slightly~~ smaller than the local ~~laminar~~ BL thickness in order to trigger transition while avoiding a disproportionate drag increase or even turbulent separation. Next to trip wire or carborundum paper, ZZ tape facilitates the comparability between different measurement methods. Moreover, it is applied to evaluate the sensitivity of airfoils to the adverse effects of leading edge roughness (LER) ~~effects~~, as discussed by van Rooij and Timmer (2003), Timmer and Schaffarczyk, (2004) and in greater detail by Wilcox et al. (2017). Another example is Oerlemans et al. (2009), who implemented ZZ tape on the rotor blades of a commercial multi MW ~~research~~ wind turbine~~s~~. In fact, LER due to erosion and the accumulation of sediments are major challenges for rotor blade manufacturers and wind turbine operators, see Figure 2b. ~~According to Maniaci (2020),~~ Over time, LER is practically inevitable. According to Maniaci (2020), it mainly affects the mid to tip region, where the rotor blade is exposed to the highest relative velocities. Depending on ~~the severity, or~~ the degree of roughness, the AEP decrease of multi MW HAWTs is between of 2 % and 5 %.

Commented [D7]: RC2: commercial instead of research wind turbine

~~A fundamental difference between GFs and VGs is that the latter, if installed in proximity to the leading edge, can also be used to control the boundary layer flow even at low angles of attack (AoA) [Q] that is typical for the inboard region of a blade.~~

Formatted: Highlight

As opposed to GFs, VGs have been commercialized by various wind energy companies for almost two decades. Usually, the suboptimal or declining AEP motivates blade manufacturers and wind park operators to investigate possible causes, such as

~~As opposed to GFs, VGs have been commercialized by various wind energy companies for almost two decades. The suboptimal or declining AEP over the years is often the reason for blade manufacturers and wind park operators to investigate the possible causes, such as early separation or LER, and to invest in feasible solutions, such as PFC devices. VGs are implemented in order to prevent, or at least to alleviate, the flow separation in the root to mid region of rotor blades. More recent studies have investigated the opportunities of relatively small VG heights in the mid to tip blade region, see Bak et al. (2018). According to Lin (2002), they are referred to as sub- BL or low profile VG configurations, see Sect. 2.5. Typically, VGs are commercialized as retrofit solutions, i.e. add-ons that are installed onto the surface of already running rotor blades, as depicted in Figure 2a. In this way, SMART BLADE (2021) predict an AEP growth of approximately 2%. A more detailed review on VGs for use on rotor blades is provided by Bak et al. (2016) and González-Salcedo et al. (2020).~~

Commented [D8]: RC2: improve sentences

(a) (b)

Figure 2. Utility scale wind turbines. (a) Simultaneous flow tuft measurements ~~on different blades of the same rotor (~~, baseline versus VG configuration~~)~~, on the same rotor, with permission from SMART BLADE GmbH. (b) Leading edge erosion at the blade tip, with permission from Seilpartner GmbH.

~~early~~ separation or LER. One possible solution is the installation of VGs to alleviate the flow separation in the root to mid region of rotor blades. More recent studies have also investigated the opportunities of relatively small VG sizes towards the tip region, see Bak et al. (2018). Typically, VGs are commercialized as retrofit solutions, i.e. add-ons that are installed on the surface of already running rotor blades, as depicted in Figure 2a. In this way, SMART BLADE (2021) predict an AEP growth of approximately 2%. A more detailed review on VGs for use on rotor blades is provided by Bak et al. (2016) and González-Salcedo et al. (2020).

The purpose of VGs is to delay the BL stagnation and thus separation, see Figure 2a. As such, the flow tufts are attached to the blade surface, as compared to the stalling baseline blade. The thin vanes shed a pair of vortices transporting momentum from the more energetic flow into the viscous layers close to the surface. The vortex system spreads out towards the TE, where it is released into the wake. More detailed research on the mechanism of VGs is provided by Manolesos and Voutsinas (2015). ~~The purpose of VGs is to delay the stagnation of the BL flow and thus separation. Installing VGs, Figure 2a illustrates that the flow tufts are attached to the blade surface until closer to the TE, as compared to the stalling baseline blade. The thin vane tips shed a pair of vortices in order to transport momentum from the free flow into the viscous BL close to the surface. The vortex system spreads out towards the TE, where it is released into the immediate wake. More detailed research on the underlying mechanism of VGs is provided by Manolesos and Voutsinas (2015).~~ Overall, the VG effect is quantifiable as a substantial increase in both maximum lift~~, $c_{l,max}$~~ and the AoA where stall is initiated, $\alpha(c_{l,max}) = \alpha_{cl,max}$. ~~However~~At the same time, drag is increased significantly at low and moderate AoA. The impact on the aerodynamic efficiency, L/D (α), depends on the design parameters that are ~~-~~summarized ~~illustrated~~ in Figure 3.

Commented [D9]: RC2: sentences were improved, i.e. paragraph was rewritten

Commented [D10]: RC2: idem

Commented [D11]: RC2: idem

(b)

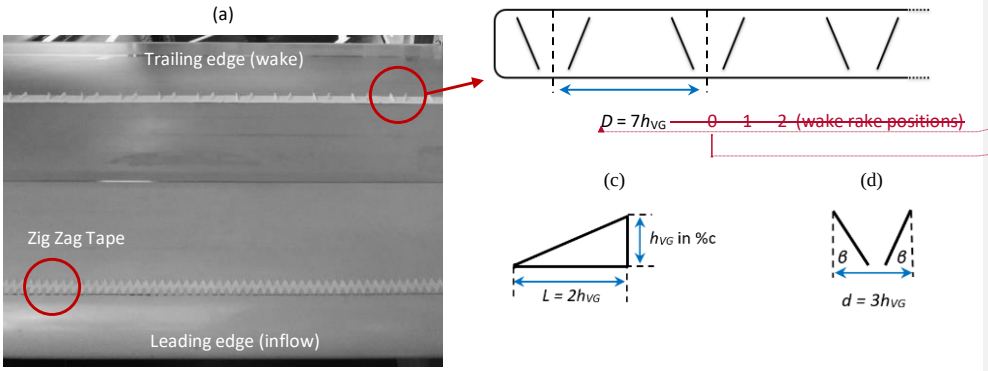

Figure 3. NACA63(3)618 during wind tunnel tests. (a) Top view on suction side with ~~Zig Zag~~ZZ tape and VG array. (b) VG panel including spacing between VG~~s centers and measurement positions of the wake rake~~, with permission from SMART BLADE GmbH. (c) Side view of single vane. (d) Top view of ~~pair of vanes~~single VG.

Figure 3a and b depict an array of VG panels, as ~~it is~~ installed on the suction side of the airfoil model~~airfoil SuS throughout the wind tunnel tests, see Sect. 3 and 4.~~. Following ~~Timmer and van Rooij (2003) and~~ Baldacchino et al. (2018), the design parameters generate a counterrotating, common downflow VG system. The spacing between the center points of two VGs is defined as $D = 7h_{VG}$, see Figure 3b. ~~According to~~ Figure 3c shows that ~~,~~ each VG consists of a delta-shaped pair of vanes with a ~~uniform~~ length, $L = 2h_{VG}$, and ~~a certain~~ the VG height, h_{VG}, given in %c. According to Figure 3d, ~~shows that~~ the distance between the two vanes, ~~is~~ $d = 3h_{VG}$, results in ~~facing each other in an angle~~ $\beta \approx \pm 18°$. ~~Furthermore, the spacing between the center points of two VGs is $D = 7h_{VG}$, see Figure 3b. The positions 0, 1 and 2 indicate the spanwise wake rake locations, as discussed in Sect. 4.2.3.~~

1.5 Combining Vortex generators and Gurney flaps

Despite the large body of literature on ~~both~~ each ~~PFC~~ devices, the simultaneous use of GFs and VGs is less profoundly researched. Storms et al. (1994) investigated one such configuration in the NASA Ames Research Center ~~based on the~~ using a NACA4412 profile ~~at $Re = 2{\cdot}10^6$. Combining $h_{GF} = 1.25$ %c with $h_{VG} = 0.5$ %c at $x_{VG} = 12$ %c and a spacing between the VGs of $D = 6h_{VG}$, ,~~ ~~s~~Stall ~~is~~ was delayed by around 5° and $c_{l,max}$ ~~is~~ was increased by 36 % improving L/D at elevated AoA. However, at low and moderate AoA, the combined drag penalty ~~leads~~ led to ~~reduced~~ decreased ~~L/D (α)~~ aerodynamic efficiency. Fuglsang et al. (2003) conducted ~~extensive research~~experiments ~~based on the Riso-B1-24~~ in the VELUX wind tunnel of the DTU based on the Riso-B1-24. ~~at $Re = 1.6{\cdot}10^6$.~~ To the authors' knowledge, this is the only experimental study applying VGs and GFs on a dedicated wind turbine airfoil. ~~The Riso-B1 family is dedicated to rotor blades of multi MW wind turbines. The tested configurations consisted of $h_{GF} = 1$ %c combined with $h_{VG} = 1$ %c at $x_{VG} = 20$ %c and $D = 4.2h_{VG}$ delaying s~~Stall~~eparation~~ was delayed by approximately 3°, coupled with an increase in $c_{l,max}$ of 34 %. ~~Additionally, ZZ tape was applied~~

Formatted: English (United States)

Commented [D12]: RC2: Indication of wake rake positions was deleted to avoid confusion

Commented [D13]: RC2: The content of this paragraph was summarized and shortened.

Commented [D14]: Q1(major): The section was rewritten highlighting the novelty of this study in comparison to the given references

Formatted: Font: Not Italic

Formatted: Font: Not Italic

Formatted: Font: Not Italic

~~about a 4% increase in $c_{l,max}$ and a 9% decrease in $c_{d,min}$ at $Re = 3 \cdot 10^6$. Applying VGs alone approximately increased $c_{l,max}$ by 2%. Similar results were achieved by Zhang et al. (2014) and Fuglsang et al. (2014).~~ Godard et al. (2009) found that, despite ~~a~~ the small *L/D* decrease, the combination of both devices *"(…) could provide an attractive choice for the root part of wind turbine blades where control of lift is the dominant design driver."* ~~Both devices were designed and manufactured for the DTU 10MW RWT airfoil DTU-W-A21 at $Re = 12 \cdot 10^6$.~~ Fuglsang et al. (2014) ~~and Godard et al. (2009)~~ in a recent study Li-shu et al. (2013) performed ~~experiments~~ wind tunnel tests on ~~the~~ a WA251A airfoil ~~airfoil~~ at the Northwestern Polytechnical University of Xi'an. ~~at $Re = 3 \cdot 10^6$. Applying Maximum lift $h_{GF} = 0.9\%c$ and $1.25\%c$ together with $h_{VG} = 0.5\%c$ at $\alpha_{VG} = 21°$ $c_{l,max}$ is~~ was increased by 18.6% delaying stall by approximately 2°. The authors report "remarkable improvements" implementing both PFC devices simultaneously. For clarity, the design parameters of the mentioned references are summarized in Table 1~~.~~.

Table 1. Literature references. GF and VG design parameters.

Airfoil	Reference	Re [$\cdot 10^6$]	h_{GF} [%c]	h_{VG} [%c]	α_{VG} [°]	D [h_{VG}]
NACA4412	Storms et al. (1994)	2.0	1.25	0.5	12	6.0
Risø-B1-24	Fuglsang et al. (2003)	1.6	1.0	1.0	20	4.2
WA251A	Li-shu et al. (2013)	3.0	0.9, 1.25	0.5	21	unspecified

~~In all mentioned reports of this section, the combined effect of GFs and VGs appears to be beneficial compared to the corresponding VG (only) configuration.~~

The literature review shows that GFs, ZZ tape and VGs are well-studied PFC devices. However, to the authors' knowledge, there are no scientific reports investigating MGF heights smaller than 0.5%c and their combination with VGs for use on dedicated wind turbine airfoils. This study aims at closing these research gaps. ~~The aerodynamic effects of either GFs or VGs on the airfoil performance is well documented in literature. To the authors' knowledge, available contributes in closing these knowledge gaps Various wind tunnel studies emphasize the benefits of very small GFs, so called MGFs, particularly in terms of the aerodynamic efficiency. However, the simultaneous installation of GFs and VGs is less profoundly researched.~~

2. Airfoil simulations

In preparation for the wind tunnel tests, the simulation software XFOIL is used to determine the appropriate ~~dimensions~~ size of each PFC device in relation to the local boundary layer thickness of the corresponding airfoil.

2.1 Airfoils

Figure 4a ~~shows~~ displays the two airfoils that are tested ~~throughout~~ during the wind tunnel experiments, ~~:~~ the NACA63(3)618, ~~the AH93W174~~ and the DU97W300. They are applied at different sections of large rotor blades, see Figure 4b. The main ~~airfoil~~ specifications are summarized in Table 2.

(a)

Commented [D15]: RC2: The information of this paragraph were presented in a more lucid table

Formatted: Font: 9 pt, Not Bold

Formatted: Font: 9 pt, Not Bold, Italic, Not Superscript/ Subscript

Formatted: Font: 9 pt, Not Bold

Formatted Table

Formatted: Font: 9 pt

Formatted: Left

Formatted: Font: 9 pt

Formatted: Left

Formatted: Font: 9 pt

Formatted: Left

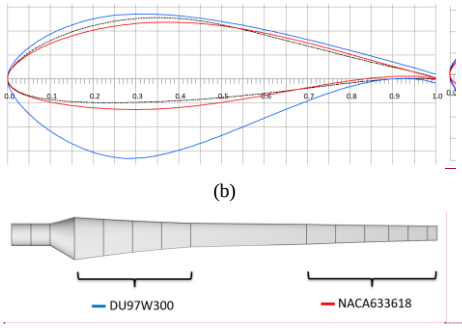

Figure 4. NACA63(3)618 and ~~, AH93W174,~~ DU97W300. (a) Airfoil coordinates normalized by the chord length. (b) ~~Position of airfoils~~ Airfoil position on a generic rotor blade.

Table 2. Maximum thickness, maximum camber and trailing edge thickness. Chord position in brackets. All values in %c.

Airfoil	$h_{th,max}$ (x)	$h_{camber,max}$ (x)	h_{TE}
NACA63(3)618	18.0 (34.0)	3.0 (53.7)	0.17
~~AH93W174~~	~~17.4 (33.0)~~	~~4.0 (38.0)~~	~~0.33~~
DU97W300	30.0 (29.3)	2.1 (80.5)	1.75

The NACA63(3)618 is part of the six-digit wing sections developed by the National Advisory Committee for Aeronautics (NACA) for use on high speed aircrafts, see Abbott and von Doenhoff (1959). The NACA 63 and 64 families are still popular for the design of large rotor blades, ~~especially in the mid to tip region,~~ see Timmer (2009). ~~The NACA63(3)618 is characterized by a relatively high lift and low drag performance due to the extended laminar BL. The main downside is the sensitivity to roughness effects, as shown in Sect. 4.1.1. The AH93W174 is a wind turbine airfoil for the mid to tip blade region developed by the Institut für Aerodynamik und Gasdynamik (IAG) at Stuttgart University, see Althaus (1996). Compared to the NACA63(3)618, the maximum thickness is similar, but the maximum camber is higher, thus leading to a steeper lift slope. Furthermore, L/D_{max} is shifted towards more elevated AoA covering a relatively wide range of high performance. However, the aerodynamic efficiency is degraded by the effect of forced LE transition, see Sect. A1.~~ The DU97W300 was designed by the Delft University (DU) as a dedicated wind turbine airfoil ~~is dedicated to the root to mid blade region, developed by the Delft University (DU)~~, see Timmer and van Rooij (2003). ~~It is characterized by the limited upper surface thickness and relatively low maximum camber, see Figure 4a. Therefore, the pressure recovery is milder avoiding premature separation on the suction side, while improving its sensitivity to roughness effects, see Sect. 4.2.1. The lift penalty is compensated for by the pronounced S- shape of the PS contour approaching the TE, as explained by van Rooij and Timmer (2003). In fact, this aft-loading tail changes the flow field in a similar way than the GF, as previously discussed in Sect. 1.2.~~

Commented [D16]: RC2: AH93W174 was removed for brevity

Formatted: Font: Not Bold

Formatted: Font: Not Bold

Formatted: Font: Not Bold

Formatted: Font: Not Bold

Commented [D17]: RC2: Excessive information on airfoils was removed

2.2 XFOIL simulations

The 2D airfoil performance is simulated with the panel code XFOIL. ~~developed by Drela (1989).~~ The freely available and widely recognized software is based on a~~n~~ viscid-inviscid interaction scheme, which was validated, ~~amongst many others~~for instance~~,~~ by Timmer and Schaffarczyk (2004) ~~and Fuglsang et al. (2004)~~. Apart from the airfoil coordinates~~,~~, including the finite TE thickness, the software requires the chord-based Reynolds number~~,~~ ~~here $Re = 1.5 \cdot 10^6$~~ and the AoA range as input parameters, here $Re = 1.5 \cdot 10^6$ and ~~here~~ $-5° < \alpha < 20°$~~, as input parameters~~. The location of the free ~~laminar-to-turbulent~~ BL transition is modeled by means of the e^N method. The amplification factor, or N criterion, describes the level of both the surface roughness and the inflow turbulence intensity. The default value, N = 9, refers to clean conditions, i.e. assuming a completely smooth surface and laminar inflow conditions that are found in low turbulence wind tunnels. In this study, N = 5 is chosen to account for the measured ~~relatively strong~~ turbulence intensity ~~of approximately 0.3%, see Sect. 3.1~~ of the current wind tunnel facility.~~,~~ In the so-called tripped case, the transition location is fixed at a static chordwise position, x_{ZZ}, on both the ~~SuS and the PS.~~ suction and the pressure side.

$$\delta \approx 3\delta^*. \quad (1)$$

Eq. (1) is also valid for thin airfoil shapes. According to Baldacchino et al. (2018), the turbulent BL thickness is related to δ* and the momentum thickness θ,

$$\delta \approx \theta\left(3.15 + \frac{1.72}{\left(\frac{\delta^*}{\theta}\right)-1}\right) + \delta^*. \quad (2)$$

2.3 Zig Zag tape

The baseline configurations include both the free and the forced BL transition. In the ~~so-called~~ tripped case, ZZ tape is applied alongside the complete airfoil span on both the ~~SuS and the PS~~suction side (SuS) at x_{ZZ} = 5 %c and at the pressure side (PS) at x_{ZZ} = 10%c, as ~~shown~~ illustrated in Figure 3a.~~,~~ The ZZ tape height is selected in relation to the laminar BL thickness, see Eq. (1 ~~), at~~), ~~the~~ corresponding chord positions, x_{ZZ}~~, x_{ZZ}~~, and ~~and~~ the design AoA, $\alpha_{opt} = \alpha\ (L/D_{max})$, ~~so that~~

$$h_{ZZ} \leq \delta(\alpha_{opt}, x_{ZZ}). \quad (3)$$

~~$\leq 3\delta^*(\alpha_{opt}, x_{ZZ})$,~~

~~where $x_{ZZ,SuS}$ = 5 %c and $x_{ZZ,PS}$ = 10 %c.~~

Table 3. XFOIL simulations of the boundary layer thickness according to Eq. ~~(1 (~~ 1).

	α_{opt} [°]	δ_{SuS} [mm]	δ_{PS} [mm]
NACA63(3)618	5	0.51	0.55
DU97W300~~AH93W174~~	~~9~~7	0.54~~0.53~~	0.42~~0.53~~
~~**DU97W300**~~	~~9~~	~~0.54~~	~~0.42~~

Commented [D18]: RC1 (Q2major): The statement was rephrased avoiding the term “strong turbulence intensity”.

Formatted: Font: Italic

Formatted: Font: Italic

Formatted: Font: Italic

Formatted Table

Formatted: Justified

~~According to~~ Based on Table 3, ~~and applying~~ Eq. (3) and Eq. (3), the NACA 63(3)-618 ~~and the~~ AH 93 W 174 ~~are both~~ is equipped with h_{ZZ} = 0.4 mm and the DU 97 W 300 with h_{ZZ} = 0.3 mm. ~~As~~ such, the ZZ tape penetrates the upper layers of the BL without increasing drag excessively. The width of the turbulator tape is 12 mm and the angle between its serrations is 60°. These characteristics are in close agreement with comparable wind tunnel tests at the DU and the DTU, see Timmer and van Rooij (2003) and Fuglsang et al. (2004). ~~Sect. 4.~~

Formatted: Font: Italic

Formatted: Font: Italic

Commented [D19]: RC2: The selection of the ZZ height was explained with more clarity.

2.4 Mini Gurney flaps

Kentfield (1996), Giguère et al. (1997) and Bechert et al. (2000) postulated that the GF needed to be covered by the local BL in order to avoid an excessive drag, in relation to the lift increase. Following from that, ~~Previously, the~~ Alber et al. (2017) ~~authors reviewed~~ evaluated wind tunnel ~~studies~~ data of ~~9~~ different DU and NACA airfoils at $1 \cdot 10^6 < Re < 2 \cdot 10^6$. It was concluded that L/D (α) could only be maintained or improved using very small GFs in the range of $0.2\ \%c \leq h_{GF} \leq 0.5\ \%c$, i.e. GFs that were submerged deeply into the local BL. However, the BL thickness depends on the interaction of multiple factors, such as the Reynolds number, the AoA and the transition location. Hence, the definition of a ~~$\frac{h_{GF}}{\delta}$~~ ~~the current XFOIL simulations~~ MGF hereby refers to a height of between one and two times the local BL displacement thickness at the design AoA,

$$\delta^*(\alpha_{opt}) \leq h_{MGF} \leq 2\delta^*(\alpha_{opt}). \quad (4)$$

Within the range given by Eq. (4~~4~~), the MGF effect on the airfoil performance is assumed to be beneficial throughout the pre-stall region, as further investigated by means of the wind tunnel measurements, see Sect. 4. Moreover, combining Eq. (2) and Eq. (4~~4~~), an appropriate MGF height may also be estimated as approximately one quarter of the turbulent BL thickness,

$$h_{MGF} \approx 0.25\delta(\alpha_{opt}). \quad (5)$$

Table 4. XFOIL simulations of the boundary layer displacement thickness and the resulting MGF heights according to Eq. (4~~4~~). ~~for $c_l, c_d > 0$.~~

~~Following from Eq. (7), the definition of a MGF hereby refers to an effective height of between one and two times the local δ* at the design AoA, so that~~

~~$$\delta^*(\alpha_{opt}) \leq h_{MGF} \leq 2\delta^*(\alpha_{opt}).$$~~ ~~(8)~~

~~For $h_{MGF} < \delta^*$, the impact of the MGF on the airfoil performance becomes insignificant. Combining Eq. (2) and Eq. (8), an appropriate MGF height is estimated to be in the order of one quarter of the turbulent BL thickness at the TE,~~

~~$$h_{MGF} \approx 0.25 \cdot \delta(\alpha_{opt}).$$~~ ~~(9)~~

~~Within the boundary condition given by Eq. (8) and Eq. (9), the impact of a MGF appears to be beneficial in terms of the lift performance, the stall behavior and the aerodynamic efficiency, as further discussed in Sect. 4. For $h_{MGF} < \delta^*$, the impact of the MGF on the airfoil performance becomes insignificant.~~

~~Table 3. XFOIL simulations of the boundary layer thickness according to Eq. (2).~~

Formatted: Normal

Formatted: Normal

Formatted: Caption

Field Code Changed

	clean		ZZ	
	α_{opt} [°]	α_{opt} [°] δ^*_{clean} [%c]	h_{MGF} [%c]	δ^*_{ZZ} [%c]	δ^*_{ZZ} [%c] h_{MGF} [%c]
NACA63(3)618	5	5 0.17	0.17…0.34	0.28	2.070.28…0.56
DU97W300AH93W174	9	7 0.250.11	0.25…0.50	0.350.23	0.35…0.701.66
DU97W300	9	0.25		0.35	2.85

Table 44 shows that According to Table 3 and applying Eq. (8) and Eq. (9), the MGFs h_{MGF} is case dependent on the airfoil itself and on whether transition is free or fixed. In the latter case, are in the range of 0.1 %c < h_{MGF} < 0.7 %c. It is reiterated that δ^* increases significantly in case of forced LE transition δ^*_t is increased significantly due to the early expansion of the turbulent BL. This observation is crucial when applying MGFs in order to compensate for the decambering effects of ZZ tape, as discussed in Sect. 4 and 5. For the purpose of the current wind tunnel tests, the following flap heights are installed: In summary, h_{MGF} = 0.25%c, , 00.5 %c and andh_{GF} = 1 %c are implemented, as such covering both the clean and the tripped cases. Even though it is not considered a MGF as per Eq. (4), h_{GF} = 1 %c to cover for both the clean and the tripped baseline cases. It is noted that h_{GF} = 1 %c is included as a common literature reference. is not considered a MGF configuration as per Eq. (8). All testedUnless specified otherwise, the GFs consist of standard rectangular, i.e. and equilateral angle profiles made of brass. with an ascending wall thickness of 0.3 mm, 0.5 mm and 0.6 mm, in relation to the size of the GF.

2.5 Vortex generators

In general, tThe chord position of the VG array, x_{VG}, is located upstream of the mean separation line , $x_{sep}(\alpha_{cl,max})$, in order to delay stall, $x_{sep}(\alpha_{cl,max})$, and downstream of the BL transition location , $x_{tr}(\alpha_{opt})$, in order to minimize limit the drag penaltyat pre-stall operation, $x_{tr}(\alpha_{opt})$, so that $x_{tr}(\alpha_{opt}) < x_{VG} < x_{sep}(\alpha_{cl,max})$. . TheApplying Eq. (2), the VG height is determined in relation to in relation to the turbulent BL thickness on the SuSat maximum lift, i.e. at the initiation of stall, ,

$$h_{VG} \geq f\left[\delta\left(x_{VG}, \alpha_{cl,max}\right)\right]\delta(x_{VG}, \alpha_{cl,max}). \quad (6)$$

It is noted that XFOIL simulations are of low order, especially for AoA close to stall. Nonetheless, the estimation of the BL thickness is considered to be sufficiently accurate for the purpose of the current VG design.

Table 5 shows that $\delta(x_{VG})$ is similar in both the clean and the tripped cases at maximum lift, i.e. as stall is initiated. Based on Eq. (6), the VG height of h_{VG} = 1.1%c is selected. In case of the DU97W300, $h_{VG} > \delta(x = 30\,\%c)$ resembles a standard VG array in the root to mid region of a rotor blade. Regarding the NACA63(3)618, a sub boundary layer VG configuration is

Formatted: Font: Bold
Formatted Table
Formatted: Font: Bold, Not Italic
Formatted: Font: Italic
Formatted: Subscript
Formatted: Superscript
Formatted: Superscript
Formatted: Font: Times New Roman, Not Italic
Commented [D20]: RC1 (Q9major): For clarity, the range of the MGF heights was specified and included in the Table
Formatted: Font: Italic
Formatted: Font: 10 pt, Italic
Formatted: Font: 10 pt
Formatted: Font: 10 pt
Commented [D21]: RC1 (Q13major): the misleading term "at stall" was replaced

investigated with $h_{VG} < \delta(x = 50\ \%c)$, as discussed by Lin (2002) and Bak et al. (2018). In the mid to tip blade region, the objective is to reduce drag and to maintain *L/D* (α) on a high level.

Table 5. XFOIL simulations of the boundary layer thickness according to Eq. (2).

	$\alpha_{cl,max}$ [°]	x_{VG} [%c]	$\delta_{clean}(x_{VG})$ [%c]	$\delta_{ZZ}(x_{VG})$ [%c]
NACA63(3)618	12	50	1.55	1.62
~~**AH93W174**~~	~~11~~	~~30~~	~~0.64~~	~~0.66~~
DU97W300	12	30	0.58	0.72

~~Table 4 shows that, *at stall*, δ is similar in both the clean and the tripped cases. Based on Eq. (6), an uniform VG height of h_{VG} = 1.1%c is selected, including the thickness of the base panel, see Figure 3b. In case of the DU97W300 *and the AH93W174*, x_{VG} = 30%c resembles a standard VG array in the root to mid region of rotor blades. Regarding the NACA63(3)618, a tip VG configuration is investigated at x_{VG} = 50%c, where $h_{VG} < \delta$ in order to reduce additional drag. Next to the effect of stall delay, the primary objective is to maintain *L/D* (α) on a high level in the mid to tip blade region. According to Lin (2002), the optimum height of sub-BL or low-profile VGs is in the range of 20%$\delta < h_{VG} <$ 50%δ.~~

2.6 Summary

Figure 5a displays both the height and the chordwise location of each PFC device that is investigated in this section. According to previous research efforts at the TU Berlin, Figure 5~~b and Figure 5~~b and c~~e~~ depict the vorticity caused by either VGs or MGFs~~, according to previous research efforts at the HFI of the TU Berlin.~~ The wake interaction of the flow control mechanisms and its effects on the lift and drag performance is ~~tested~~ presented as part of the wind tunnel ~~campaign~~tests in Sect.4~~, as described in the following sections of this report.~~.

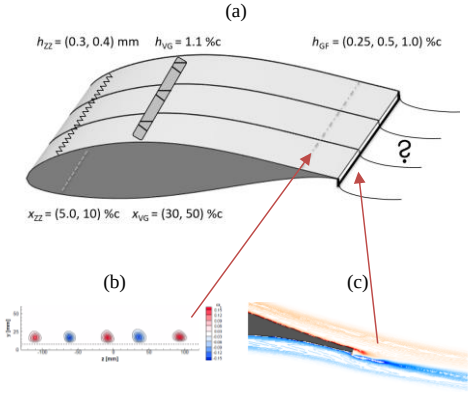

Formatted Table

Commented [D22]: RC1 (Q13major): the misleading term "at stall" was replaced

Formatted: Font: Italic

Formatted: Font: Italic

Formatted: Font: Italic

Figure 5. (a) Height and location of passive flow control devices. (b) ~~PIV~~ Particle Image Velocimetry (PIV) measurements of VG vortices on the NACA63(3)618 in spanwise view (h_{VG} = 1.7%c at x_{PIV} = 80%c and Re = 1.3·10^6), reproduced from Mueller-Vahl et al. (2012). (c) CFD simulations of a ~~M~~MGF~~ini Gurney flap~~ on the HQ17 in side view (h_{GF} = 0.5%c at α = 44.0° and Re = 1·10^6), reproduced from Schatz et al. (2004a).

3. Experimental set-up

The wind tunnel test section, the measurement methods and the data reduction process are specified, including the force balance for the lift, and the wake rake for the drag measurements at a ~~constant~~ Reynolds number of Re = 1.5·10^6.

3.1 Test section

The experiments are conducted in the large closed-loop wind tunnel of the HFI at the TU Berlin. The airfoil test section is 2 m in width and 1.44 m in height. It consists of a 2.5 m long removable structure~~, the so-called airfoil box, which~~ that is attached to the duct outlet, see Figure 6a. The contraction ratio is 6.25:1 and the complete length of the test section is 5 m. ~~Between 1998 and~~ In 2000, the airfoil box was

~~[illegible]~~

(a) (b)

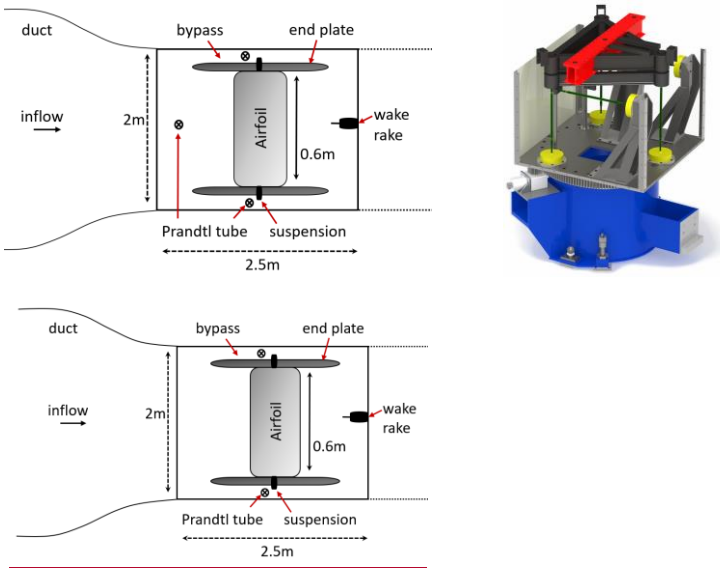

Figure 6. (a) Airfoil test section in top view. (b) Force balance underneath the test section in side view, load cells in yellow, support for attaching. the frame of the wing model in red.

Commented [D23]: RC1(Q4minor): The term "airfoil box" was replaced

Commented [D24]: RC2: Additional information on the test section was removed.

Formatted: English (United States)

Formatted: English (United States)

Formatted Table

Formatted: Centered

Formatted: Centered

Commented [D25]: RC1(Q6minor): The attachment of the wing model to the force balance was specified

The inlet and the outlet of the duct walls are equipped with a ring line of pressure taps. ~~T~~The inflow velocity is determined from the contraction ratio and the static pressure difference between the inlet and the test section. ~~Parallel to~~ Additionally, two Prandtl tubes are installed in the bypass channels approximately ~~y/c = 10% upstream of~~ half of the airfoil model's chord length. The airfoil model, ~~wing~~ spanning the entire test section, as displayed in Figure 6a. It is enclosed by two 1.5m long, ~~smooth~~ end plates, ~~or splitter walls,~~ that are parallel to the tunnel, as such ~~in order to minimize~~ reducing the influence of the wall BL. The velocities inside the 0.25 m wide bypass channels are measured via two separate Prandtl tubes to obtain the effective inflow ~~airfoil~~ velocity. ~~The suspension is decoupled from the end plates and the tunnel walls.~~ The wing is directly ~~mounted~~ clamped to the platform of the permanently installed force balance underneath the test section, see Figure 6b. Hence, the suspension is decoupled from the end plates and the tunnel walls. The AoA is controlled by means of a stepping motor with an accuracy of 0.1°, which is ~~part~~ directly attached to ~~of~~ the suspension. The ~~airfoil~~ wing models ~~included the NACA 0018, the AH 93 W 174 and the DU 97 W 300, see Figure 4.~~ The wings were CNC milled from solid blocks of Obomodan™, as described by Pechlivanoglu (2013). The model length is 0.6 m and the span is 1.54 m resulting in an aspect ratio of 2.56.

Commented [D26]: RC1 (Q5minor): the measurement principle of the inflow velocity was specified.

RC1 (Q7minor): the dimensions of the end plates was included

RC1 (Q8minor): the reference Prandtl tube in front of the airfoil model was removed to avoid confusion

Commented [D27]: RC1(Q6minor): idem

3.2 Measurement methods

3.2.1 Force balance

The lift, ~~drag forces and side forces of the airfoil model~~ are directly transferred to the six component force balance, see Figure 6b. The load cells consists of strain gauges generating voltage signals that are proportional to the incoming forces. Each signal is digitalized by a CompactDAQ System of National Instruments with a sampling rate of 5 kHz. The data is recorded using a LabVIEW user interface, including forces, velocities and environmental conditions, i.e. air density and kinematic viscosity, all of which are automatically converted to average results at each AoA. The LabVIEW interface also contains the AoA control in terms of range, steps and measurement duration. According to Meyer et al. (2016), the uncertainty of the uncorrected lift coefficients, ~~averaged~~ $c_{law}(\alpha)$, ~~and c_d measurements~~ is 0.2%. ~~The $c_l(\alpha)$~~ As such, the lift results show good agreement with literature data, ~~as discussed in~~ as shown in Appendix B1, ~~Sect. 4.~~ However, since its implementation in the wind tunnel, the ~~current~~ set-up has been characterized by elevated ~~$c_d(\alpha)$~~ drag results. The reasons are the small gaps between the wing and the end plates leading to suction effects. Moreover, a turbulent BL is formed on the end plates triggering separation on the outer parts of the airfoil model, ~~i.e. in the vicinity of splitter walls.~~ Both effects are 3D and therefore detected in the form of increased total drag values, see Meyer (2000) and Meyer et al. (2016). For the purpose of this study, a wake rake is designed, constructed and implemented into the test section aiming at 2D drag measurements.

3.2.2 Wake rake

The wake rake method is widely recognized ~~to~~ for determining 2D drag coefficients at pre-stall conditions, see ~~Barlow et al. (1999) and the references given throughout Sect 4.~~ Fuglsang et al. (2004).

(a) (b) (c)

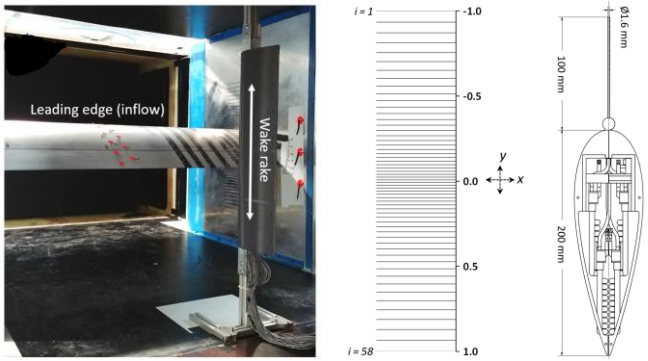

Figure 7. (a) Test section during wind tunnel measurements including airfoil model, one of the end plates and the wake rake. (b) Normalized vertical rake tube positions, *y*, and numbering, *i*, in side view. (c) Cross section of wake rake casing and pressure tube in top view.

Figure 7a ~~shows~~ displays the ~~present~~ wake rake, which is positioned ~~downstream~~ at a distance of one chord length, ie. ~~the~~ airfoil trailing edge at $x - c = 0.6$ m, downstream of the airfoil trailing edge. ~~-~~ According to Barlow et al. (1999), ~~).~~ ~~T~~ This distance of at least 70%c is necessary for the flow to return to the static pressure level in ~~side~~ the wind tunnel. ~~, see Barlow et al. (1999).~~ Figure 7b illustrates that the rake consists of a straight vertical line of 58 pitot tubes, each measuring the total pressure, p_{total}. The normalized vertical positions are defined as y = 0.0 for the center, $y_{i=1}$ = -1.0 = -250 mm for the uppermost tube and $y_{i=58}$ = 1.0 = 250 mm for the lowest tube. The total rake span is 0.5 m. The spacing between the tubes is smallest towards the center with Δy_{min} = 4 mm, and widest towards the top and the bottom with Δy_{max} = 16.5 mm, ~~ie.~~ the ~~d~~ature solution is highest towards the center. The ~~3D printed~~ casing consists of ~~the~~ a symmetrical NACA0030 profile, see Figure 7c. The distance between the LE and the orifice of each pitot tube is 100 mm, where the impact of the ~~rake~~ casing on the flow is considered negligible. The static pressure, p_{static}, is determined by means of the static pressure lines of two Prandtl tubes that are installed inside the downstream plane of the wake ~~de~~ ~~T~~ ~~T~~ ~~p~~ ~~p~~ ~~d~~ ~~d~~ ~~d

where, Δp_i is the mean differential pressure value in Pa at each rake tube, ~~The raw data is post-processed using a specific Matlab script,~~

$$\Delta\Delta\bar{p}_i p_i = \Delta p(y_i) = \Delta p_{total}\bar{p}_{total}(y_i) - \Delta p_{static}\bar{p}_{static}, \quad (8)$$

~~where ρ refers to the air density in kg/m³ and i = 1,2…58 to each rake tube~~and Δp_{ref} the ~~.~~

~~2.~~ ~~The~~ reference pressure in Pa of the free flow that is taken from ~~is calculated as the mean value of~~ the two uppermost and the two lowest rake tubes, ~~see Figure 7b, so that,~~

$$\Delta p_{ref}\Delta\bar{p}_{ref} = 0.25 \cdot (\Delta p_1\Delta\bar{p}_1 + \Delta p_2\Delta\bar{p}_2 + \Delta p_{57}\Delta\bar{p}_{57} + \Delta p_{58}\Delta\bar{p}_{58}). \quad (9)$$

The pressure coefficient, c_{pi}, is defined as,

$$c_{pi} = \frac{\Delta p_i\Delta\bar{p}_i}{\Delta p_{ref}\Delta\bar{p}_{ref}}, \quad (10)$$

~~describing the characteristic pressure loss at each AoA, see Figure 18.~~

~~3.~~ Based on Eq. (~~7~~), ~~T~~the uncorrected ~~total~~ drag contribution of each rake tube, c_{di}, becomes,

$$c_{di} = \sqrt{c_{pi}} - c_{pi}. \quad (11)$$

~~4.~~ The~~The~~ uncorrected total drag coefficient ~~, $c_{d,raw}(\alpha)$,~~ is then numerically integrated over the spacing between the rake tubes using the trapezoid rule, ~~so that,~~

$$c_{d,raw}(\alpha) = \frac{1}{c}\sum_1^{58}(c_{di} + c_{di+1}) \cdot (y_{i+1} - y_i), \quad (12)$$

where c is the airfoil chord length and y_i the normalized position of each rake tube, as illustrated in Figure 7b.

~~3.2.3 Wind tunnel correction~~

The measured ~~2D airfoil performance~~lift and drag polars, $c_{l,raw}(\alpha)$ and $c_{d,raw}(\alpha)$, are ~~is modified~~ affected by the wind tunnel walls. ~~compared to equivalent free flow conditions.~~ The reasons ~~for that~~ are~~: 1.~~, first of all, that the solid blockage effect ~~leading~~ leads to the constriction of the curved streamlines around the airfoil model. Secondly, ~~and 2.~~ the wake blockage effect ~~leading~~ causes ~~to~~ the constriction of the curved streamlines in the wake. For the results to be comparable to equivalent open flow conditions, it is necessary to apply wind tunnel corrections, as detailed in Appendix A. In the remainder of this report, the polar data refers to the corrected lift and drag coefficients, $c_l(\alpha)$ and $c_d(\alpha)$.

~~Following Barlow et al. (1999), the total blockage, ε, is the sum of the solid and the wake blockage factors,~~

$$\varepsilon = \varepsilon_{solid} + \varepsilon_{wake} = A\frac{\pi^2}{48}\left(\frac{\epsilon}{h_{wt}}\right)^2 + \frac{\epsilon}{4h_{wt}}c_{d,raw} = A\mu + \frac{\epsilon}{4h_{wt}}c_{d,raw}, \quad (16)$$

~~for ε > 0,~~

~~where A refers the so-called body shape factor, which is related to the maximum airfoil thickness, $h_{wt} = 1.44\, m_x$, which is the height of the test section. Moreover, $\mu = \frac{\pi^2}{48}\left(\frac{\epsilon}{h_{wt}}\right)^2$ is introduced as an auxiliary constant.~~

~~Based on Eq. (16), the blockage correction is applied on the following parameters at each static AoA,~~

Formatted: English (United States)

Formatted: Normal, No bullets or numbering

Field Code Changed

Commented [D33]: RC1(Q13minor): idem

Formatted: Normal, No bullets or numbering

Field Code Changed

Formatted: Normal, No bullets or numbering

Commented [D34]: RC2: Sect. 3.2.3. Wind tunnel corrections was shifted to Appendix A to shorten the main part of the report

Formatted: Normal

Formatted: Justified

Formatted: Font: Italic

~~where c_m refers to the moment coefficient at 0.25c.~~

The inflow velocity, u_{inf} = 40 m/s, corresponds to a ~~constant~~ Reynolds number of approximately $1.5 \cdot 10^6$. The free stream turbulence intensity of the empty wind tunnel is estimated ~~with the inflow~~by means of a Prandtl tube and ~~amounts~~ is~~to~~ less than 0.3 %. The AoA ranges from -5° < α < 17°~~,~~ in steps of 1°. At each static AoA, there is a buffer of 4 s for the flow to settle, after which data is recorded for another 5 s. Hence, the total number of samples is $n = 5 \cdot 10^4$ for each rake sensor and $n = 2.5 \cdot 10^4$ for the load cells ~~for each load cell~~ of the force balance. Before each test run, all sensors are subjected to a zero-offset measurement at standstill in order to reduce experimental errors.~~.~~

4. Experimental results

The presentation of the wind tunnel ~~results~~ measurements is focused on ~~are presented separately for~~ the NACA63(3)618 with GFs ~~(mid to tip blade region)~~ and the DU97W300 including VGs plus GFs. ~~(root to mid blade region). For clarity, the results of the AH93W174 are included as Appendix A. The baseline~~All results refer to ~~measurements consist of~~ the clean and the tripped cases. They are presented in the form of both the polar curves and the wake pressure fields. ~~compared to literature data in order to validate the experimental set-up. Next, different combinations of MGFs and VGs are assessed by means of characteristic parameters, i.e. the lift performance, the stall behavior and the aerodynamic efficiency.~~

4.1 NACA63(3)618: Gurney flaps

4.1.1 Polar curves

~~where $n = 5 \cdot 10^4$ is the number of samples of each pressure sensor and $\Delta\bar{p}_t$ refers to the average differential pressure at each~~ ~~FigAre 8c Eqw(11e),~~clean and the tripped polar curves of the NACA63(3)618. For clarity, characteristic lift and *L/D* values are summarized in Table 6~~6~~**Error! Reference source not found.**.

In the baseline cases, the drag results are valid until stall at $\alpha_{cl,max}$ = 10.5° and the lift curves are measured until the post-stall AoA of 18.5°, see Figure 8a and c. As expected, ZZ tape with h_{ZZ} = 0.4 mm manifests itself in a lift decrease, coupled with a significant drag increase. The design point declines from $\alpha_{opt,clean}$ = 6.4° to $\alpha_{opt,ZZ}$ = 5.4° and the corresponding aerodynamic efficiency drops from $L/D_{max,clean}$ = 109 to $L/D_{max,ZZ}$ = 60, see Figure 8b and d. The clean and the tripped GF configurations are characterized by an increase in both lift and drag throughout the complete pre-stall region. Furthermore, the shape of the polar curves and the stall behaviour is maintained. In the clean cases, L/D_{max} is only marginally improved by GF025 and GF05. Nonetheless, the significant lift increase is expected to be beneficial in terms of the rotor blade performance, as long as *L/D* (α) is maintained. As such, GF025 provides the preferred results, while GF1 leads to an overall *L/D* (α) decrease. In the tripped cases, the aerodynamic efficiency is improved independently of the GF height. The reason is the significant expansion of the BL due to forced LE transition, so that larger GFs appear to be more beneficial.

Commented [D37]: RC2: The structure of this chapter was changed to shorten the report. For that, the results were restricted to

1.) the NACA63(3)618 with GFs (only) and

2,) the DU97W300 with VGs plus GFs

The following parts were moved to the appendices (pls note that the numbering of the sections and Figures has changed as they refer to the previous version of this manuscript):
- Fig. 10 + text
- 4.1.3 Vortex generators plus Mini Gurney flaps (NACA)
- 4.2.2 Mini Gurney flaps (DU97W300)

The following subsections were removed entirely (pls note that the numbering of the sections and Figures has changed as they refer to the previous version of this manuscript):
- Sect. 4.1.1 Baseline (NACA)
- Sect. 4.2.3: Fig. 17+text
- Appendix A and everything that had to do with the third airfoil AH97W174

Commented [D38]: RC1 (L377): Correct the turbulence intensity with reference ot the NASA Langley wind tunnel (this section was deleted)

Commented [D39]: RC1(Q16minor): Correct cross-reference RC2: idem

Formatted: Normal

Formatted: Normal

Commented [D40]: RC1(Q18minor): the fact that the L/D increase is marginal was highlighted

~~Figure 12. NACA63(3)618 at α = 6.4°. Gurney flaps. Standard deviation of raw pressure data over vertical wake rake positions. (a) Clean case. (b) Tripped case.~~

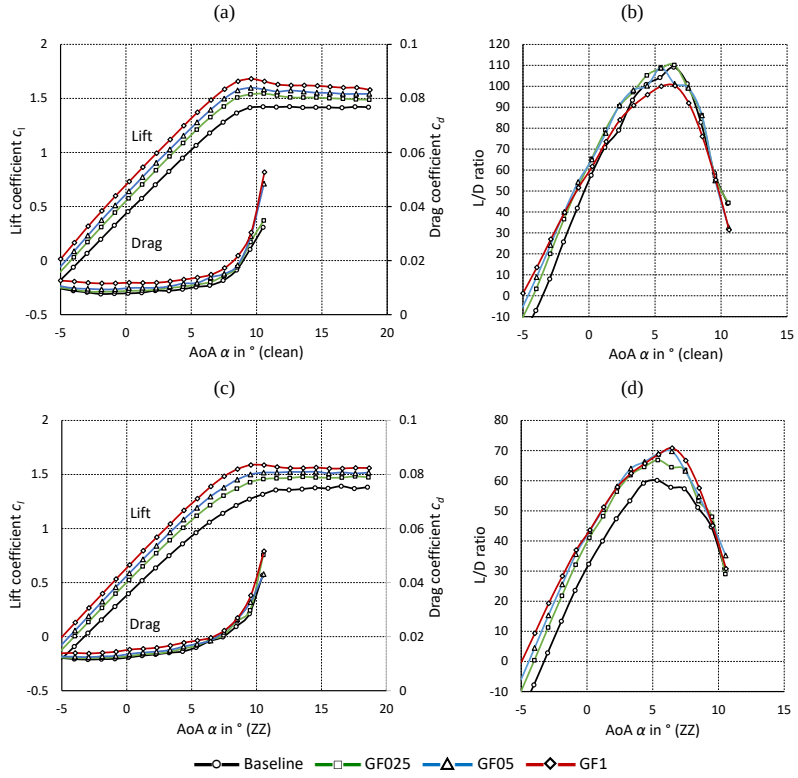

Figure 8. NACA63(3)618. Gurney flaps. (a) Lift and drag coefficients (clean). (b) L/D ratio (clean). (c) Lift and drag coefficients (ZZ). (d) L/D ratio (ZZ).

Table 6. NACA63(3)618. Gurney flaps. Characteristic values.

	Clean		**ZZ**	
	$c_{l,max}$ (10.5°)	L/D_{max} (6.4°)	$c_{l,max}$ (10.5°)	L/D_{max} (5.4°)
Baseline	1.42	109	1.32	60
GF025	1.54	110	1.46	67
GF05	1.58	101	1.52	69
GF1	1.66	100	1.59	69

~~4.1.3 Vortex generators plus Mini Gurney flaps~~

~~Figure 14. NACA63(3)618. Vortex generators and Gurney flaps. (a) Lift and drag coefficients (clean). (b) L/D ratio (clean). (c) Lift and drag coefficients (ZZ). (d) L/D ratio (ZZ).~~

4.1.2 Wake pressure field

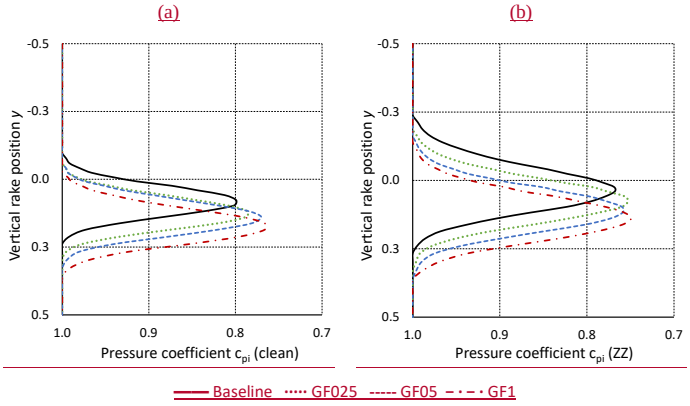

Figure 9. NACA63(3)618 at $\alpha = 6.4°$. Gurney flaps. Pressure coefficients over vertical wake rake positions. (a) Clean case. (b) Tripped case.

Next, the fluctuations of the pressure measurements indicate the intensity of the wake unsteadiness, which is an important contributor to the total drag value. These fluctuations are determined via the standard deviation of the differential pressure data in Pa at each rake tube and each AoA,

$$\sigma_{pi}(\alpha) = \sqrt{\frac{1}{n-1}\sum_1^n |\Delta p_i(t) - \Delta p_i|^2}, \quad (13)$$

where $n = 5{\cdot}10^4$ is the number of samples of each pressure sensor, $\Delta p_i(t)$ the time resolved differential pressure values in Pa and Δp_i the average differential pressure in Pa at each AoA, see Eq. (8).

Figure 10a shows that, in the clean case, the intensity of the wake unsteadiness is dependent on the GF height. Despite the offset due to the steeper downwash angle, the minima of the c_{pi} curves are similar between the clean baseline and the MGF configurations, as predicted by Bechert et al. (2000) and Schatz et al. (2004b), see Sect. 1.2. In the tripped cases, Figure 10b

Formatted Table

illustrates that σ_{pi} is more pronounced due to the thicker and more turbulent BL, whereas the relative σ_{pi} (α) contribution of the GFs appears to be minor.

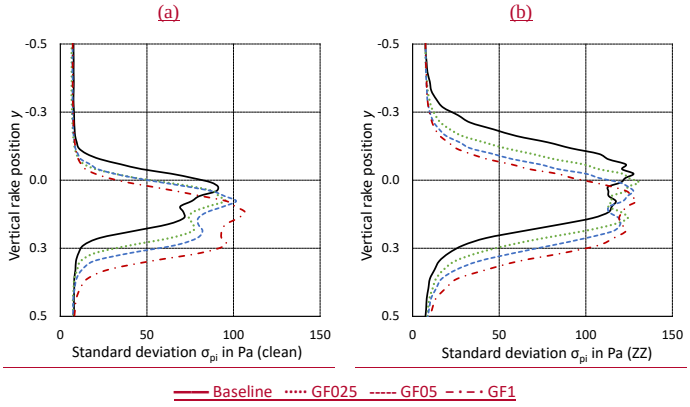

Figure 10. NACA63(3)618 at α = 6.4°. Gurney flaps. Standard deviation of raw pressure data over vertical wake rake positions. (a) Clean case. (b) Tripped case.

For completeness, additional NACA63(3)618 results are presented in Appendix B. The polar curves that refer to the combination of VGs plus GFs are included in Appendix B1. Appendix B2 presents the investigation of the different GF shapes, i.e. the rectangular versus the rectangular profiles.

4.2 DU97W300: Vortex Generators plus Gurney flaps

4.2.1 ~~Baseline~~Polar curves

Figure 11~~Figure 11~~ displays the clean and the tripped polar curves of the DU97W300. In the baseline cases, the design AoA is decreased from $\alpha_{opt,clean}$ = 9.5° to $\alpha_{opt,ZZ}$ = 7.4° and the stall angle is declined from $\alpha_{cl,max,clean}$ = 12.6° to $\alpha_{cl,max,ZZ}$ = 10.4°, see Figure 11~~Figure 11~~a and c. Hence, using ZZ tape with h_{ZZ} = 0.3 mm, separation is initiated early, in fact only 1° below $\alpha_{opt,clean}$. As a result, the aerodynamic efficiency drops from $L/D_{max,clean}$ = 88 to $L/D_{max,ZZ}$ = 41, see Figure 11~~Figure 11~~b and d. For clarity, characteristic lift and L/D values are summarized in Table 7~~7~~. Looking at the VG (only) cases, stall is delayed by approximately 3° coupled with a substantial increase in maximum lift, see Figure 11a and c. However, the VGs lead to a more abrupt stall behaviour and thus adverse load excursions, as reported by Mueller-Vahl et al. (2012). Despite the improved drag behavior at elevated AoA, the drag penalty causes L/D_{clean} to decrease at low and moderate AoA. Under tripped conditions, the aerodynamic efficiency is only slightly decreased in the lower AoA range. Furthermore, $L/D_{max,ZZ}$ is significantly increased,

Formatted Table

Formatted: English (United States)

Formatted: English (United States)

as it is shifted by almost 5° recovering a large area of otherwise separated flow between 7.4° < α < 15.6°, as illustrated in Figure 11d. In the combined cases, the VG is superposed by the GF effect leading to both stall delay and the pre-stall lift increase. Compared to the VG (only) configurations, *L/D (a)* is therefore maintained in the clean, and slightly improved in the tripped cases.

~~Figure 18. DU97W300. Pressure coefficients over vertical wake rake positions in the clean case. Vortex generators and Gurney flaps. (a) α_{opt} = 9.5°. (b) $\alpha_{cl,max}$ = 12.6°. (c) α = 16.5°.~~

~~Figure 19 displays the polar curves of all VG + GF configurations. For clarity, characteristic lift and L/D values are summarized in Table 8. The results of both the baseline and the VG (only) configurations are in very close agreement with reference measurements of the DU. Baldacchino et al. (2018) tested a comprehensive variety of VG configurations including h_{VG} = 0.8%c at x_{VG} = 30%c and $Re = 2{\cdot}10^6$. However, the tripped case consists of SuS (only) ZZ tape with h_{ZZ} = 0.17 mm at x_{ZZ} = 5.0 %c, which explains the elevated $L/D_{max,ZZ}$ compared to the current measurements, as detailed in Table 8. Next, The VG + GF configurations show that stall is delayed by around 4° coupled with a significant $c_{l,max}$ increase, again, followed by an abrupt and steep drop at stall, see Figure 19a and c. Despite the improved drag behavior at elevated AoA, the combined drag penalty causes L/D_{clean} to decrease significantly at low and moderate AoA. Overall, the results of the VG + MGFs are preferred over the VG + GF1 due to the beneficial L/D distribution, see Figure 19b. Under tripped conditions, all PFC devices are capable of maintaining L/D at low and moderate AoA. Moreover, $L/D_{max,ZZ}$ is increased as it is shifted by around 5° recovering a large area of otherwise separated flow in the range of 7.4° < α < 15.6°, see Figure 19d. Again, VG + MGFs are the preferred configurations.~~ (a)

(b)

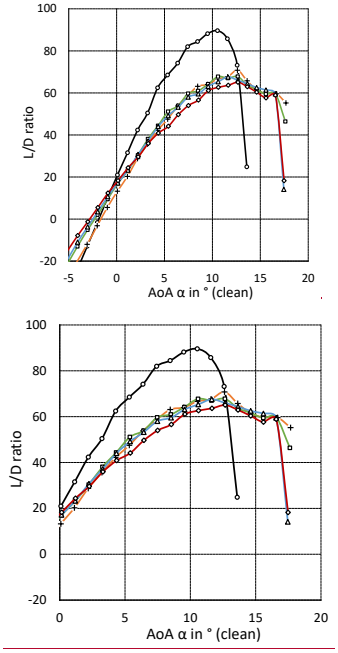

Commented [D43]: RC1(Q21minor): Paragraph was rewritten to clarify why the VG + GF cases are preferred over the VG (only) configuration

Formatted: Font color: Auto

Commented [D44]: RC2: reference is enough without repeating what it says

Commented [D45]: RC2: Restrict the validation of the measurement results to one airfoil.

Commented [D46]: RC2: rephrase.

Commented [D47]: Bett way of showing the rake position

Commented [D48]: RC1(L494): Clarify the indication of the distance between wake rake and airfoil trailing edge

Formatted: Normal

Formatted: Normal

Formatted: Normal

Formatted: Centered

Formatted Table

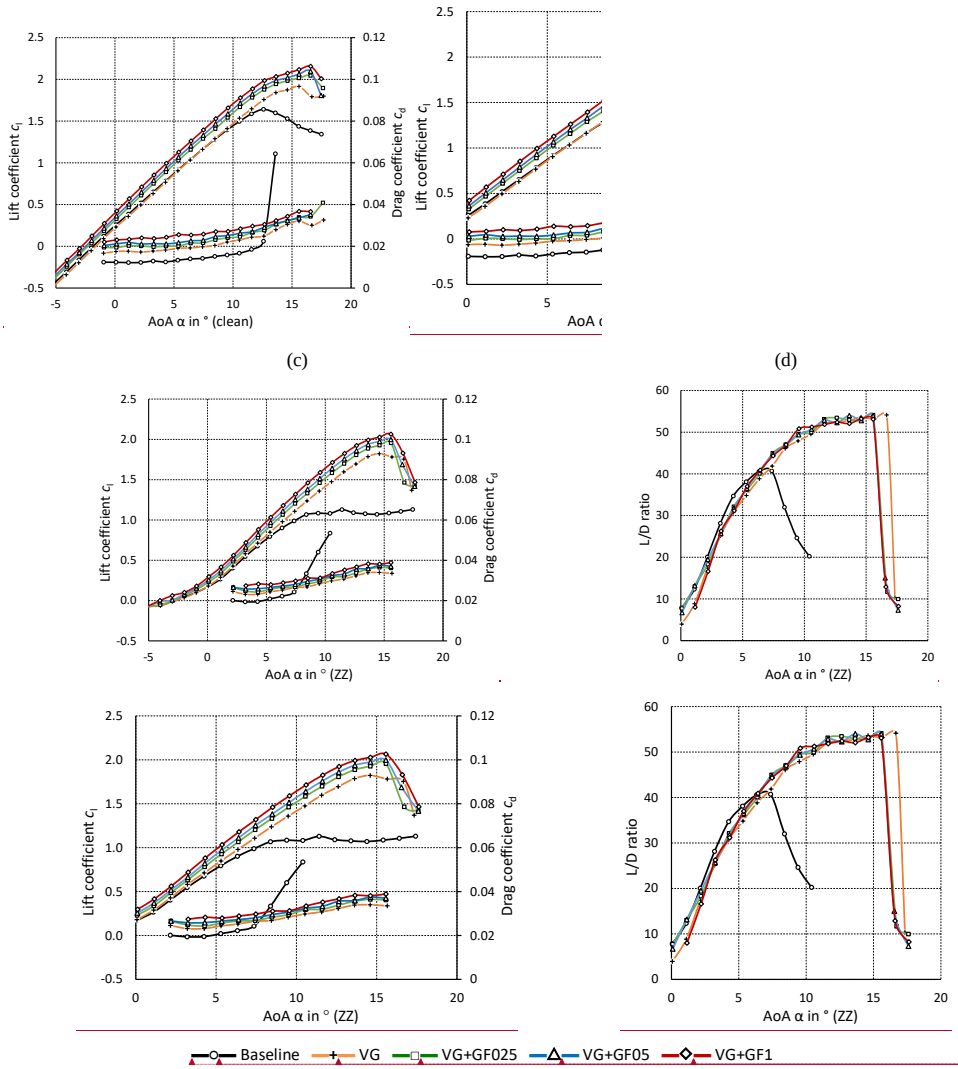

Figure 11. DU97W300. Vortex generators and Gurney flaps. (a) Lift and drag coefficients (clean). (b) L/D ratio (clean). (c) Lift and drag coefficients (ZZ). (d) L/D ratio (ZZ).

Formatted: English (United Kingdom)
Formatted: English (United Kingdom)
Formatted: English (United Kingdom)
Formatted: English (United Kingdom)
Formatted: English (United Kingdom)
Formatted: English (United Kingdom)

Table 7. DU97W300. Vortex generators plus Gurney flaps.

	Clean		ZZ	
	$c_{l,max}$ (α)	L/D_{max} (α)	$c_{l,max}$ (α)	L/D_{max} (α)
Baseline	1.64 (12.6°)	88 (9.5°)	1.13 (11.4°)	41 (7.4°)
VG	1.91 (15.6°)	71 (12.6°)	1.82 (14.6°)	52 (12.6°)
VG+GF025	2.04 (16.6°)	68 (12.6°)	1.96 (15.6°)	53 (12.6°)
VG+GF05	2.10 (16.6°)	66 (12.6°)	2.00 (15.6°)	52 (12.6°)
VG+GF1	2.16 (16.6°)	65 (12.6°)	2.06 (15.6°)	52 (12.6°)

Formatted: Font: Not Bold

~~**In summary, the DU97W300 measurements confirm the observations based on both the NACA63(3)618, see Sect. 4.1, and the AH93W174, see Appendix A: the VG is superposed by the GF effect, resulting in beneficial aerodynamic effects.**~~

Formatted: Heading 3

4.2.2 Wake pressure field

In order to deepen the understanding of the aerodynamic mechanisms, the wake rake data is further evaluated. Figure 12~~12~~a displays the pressure loss in the wake of the clean VG + GF configurations. At $\alpha_{opt,clean}$ = 9.5°, the pressure coefficients, c_{pi}, correspond to attached flow. At α = 12.6°, the wake deficit of the baseline curve extends towards the upper side of the rake indicating the formation of the TE separation bubble on the suction side and thus the initiation of stall, see Figure 12~~12~~b. The curves of the VG + GF configurations, on the other hand, show that the flow remains attached.

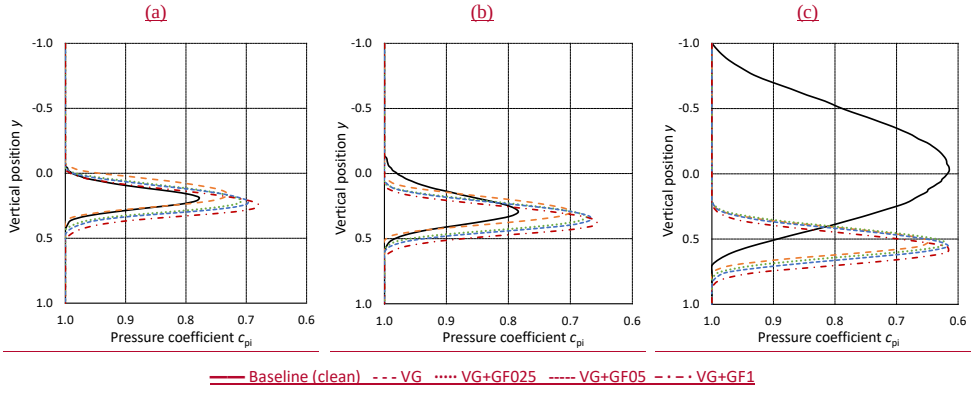

Figure 12. DU97W300. Pressure coefficients over vertical wake rake positions in the clean case. Vortex generators and Gurney flaps. (a) α_{opt} = 9.5°. (b) $\alpha_{cl,max}$ = 12.6°. (c) α = 16.5°.

At α = 16.5°, the baseline airfoil is clearly stalling, see Figure 12~~12~~c. At this point, the wake consists of separated flow, i.e. 3D structures that cannot be determined by means of the wake rake. As opposed to that, the VG configurations delay the formation of stall cells, so that the flow remains attached, as described by Manolesos and Voutsinas (2015). Finally, at α =

Commented [D49]: RC1 (Q19minor): "suppress" was replaced by "delay"

17.5°, which is not displayed here, the flow separates abruptly leading to a steep decline of the lift curves. These load excursions are perceptible in the form of strong mechanical vibrations of the setup as well as a deep roaring sound inside the wind tunnel. The wake deficit remains similar in shape and amount comparing the VG (only) to the combined configurations, again pointing towards a favorable wake interaction between VGs and MGFs.

For completeness, additional DU97W300 results are presented in Appendix C. The validation of the experimental setup is compared to wind tunnel measurements of the DU in Appendix C1. The polar curves that refer to the GF (only) configurations are included as Appendix C2.

The ~~most beneficial~~preferred ~~combination~~ configurations of VGs and GFs ~~PFC devices is~~are selected on the basis of the wind tunnel ~~results~~measurements.~~, see Sect. 4.~~ The experimental polar data is imported into the software QBlade (Marten, 2020) in order to create a generic rotor blade. The blade performance is simulated by means of two case studies, the retrofit application on an existing, and the new design application on an alternative rotor blade design. ~~-~~

5.1 Blade configurations

~~As illustrated in Figure 5a, it is reiterated that the VG and the MGF configurations refer to $Re = 1.5 \cdot 10^6$, $h_{ZZ} = 0.3$ mm and 0.4 mm, respectively, $h_{VG} = 1.1$ %c and $h_{MGF} = 0.25$%c and 0.5%c, while $h_{GF} = 1.0$ %c is not considered relevant for this section of the report.~~ Table 8 ~~demonstrates~~summarizes the qualitative effect of the prefered ~~the~~ MGF (only) and MGF+VG configurations including h_{MGF}=0.25 %c and h_{MGF}=0.5%c. ~~PFC devices on all tested airfoils by means of characteristic parameters.~~ It is noted that h_{GF}=1.0%c is not considered relevant for this section due to the elevated drag penalty and thus L/D decrease.

[Table 8] Performance evaluation of ~~Mini Gurney flaps~~ MGFs and ~~VGs vortex generators~~ based on the wind tunnel tests of the NACA 63(3)-618, ~~the AH 93W 174~~ and the DU 97W 300. ↑ for increase, ≈ for similar and ↓ for decrease.

	Clean			~~Tripped~~ZZ		
MGFs (only)	c_l ($\alpha_{~~opt~~}$) ↑	$\alpha_{cl,max}$ ≈	L/D_{max} ≈	Space c_l ($\alpha_{~~opt~~}$) ↑	$\alpha_{cl,max}$ ≈	L/D_{max} ↑
VG + MGF	c_l ($\alpha_{~~opt~~}$) ↑	$\alpha_{cl,max}$ ↑	L/D_{max} ↓	c_l ($\alpha_{~~opt~~}$) ↑	$\alpha_{cl,max}$ ↑	L/D_{max} ↑

First of all, the ~~tendencies~~effect ~~that are shown in Table 9 emphasize, first of all, that the effect~~ of ~~the~~ both PFC ~~configurations~~ devices is case dependent, as illustrated in Table 8. ~~. In~~Apart from that ~~general~~, it is difficult to measure and ~~-~~to foresee the degree of LER, as described by Papi et al. (2021). ~~For the purpose of this study~~Hence, the principal objective of this study is to improve the airfoil performance ~~in~~ based on forced LE transition ~~the tripped case~~ without jeopardizing the aerodynamic efficiency of the clean airfoil. Looking at the ~~the~~ MGF (only) configurations ~~configurations~~, lift is increased at the design point

Commented [D50]: RC2: the readability of Table was improved.

Formatted: English (United States)

Formatted Table

Formatted: Font color: Background 1

and the stall behavior is ~~basically~~ consistent. The decambering effect of the ZZ tape is partly ~~compensated for by the MGFs,~~ recovered, as such improving the aerodynamic efficiency, while $L/D_{max,clean}$ is ~~slightly improved or, at least,~~ maintained. Next, VG + MGF lead to significant improvements regarding both the lift increase and the stall delay. In the clean case, $L/D_{max,clean}$ is decreased due to the combined drag penalty. I~~i~~n the tripped case, however, ~~VG + MG~~ the combined configurations ~~F~~achieve a triple improvement ~~concerning~~ in terms of lift increase, stall delay and aerodynamic efficiency. ~~y. However, in the clean case, $L/D_{max,clean}$ decreases due to the combined drag penalty.~~

In conclusion,

5.2 Blade design

The experimental lift and drag polars are imported into the open source software QBlade. Figure 13 illustrates the rotor blade ~~design~~ of the NREL 5 MW reference wind turbine, as specified by Jonkman et al. (2009). The total rotor radius is ~~with~~ R = 63 m, ~~an~~ the average wind speed at hub height is ~~of~~ u_{avg} = 8 m/s, ~~and, according to Eq. (23), a~~. The design tip speed ratio (TSR), $\lambda(R) = \lambda_{opt} = 8$ is defined as ~~of λ_{opt} = 8, as specified by Jonkman et al. (2009).~~

$$\lambda(r) = \frac{2\pi f r}{u}, \quad (14)$$

where f is the rotational frequency in Hz.

The NREL blade is used as a template for the so-called ~~so-called generic rotor blade, which is designed in order to identify t~~generic rotor blade design, which ~~he impact of the PFC configurations on the rotor performance of an aerodynamically optimized blade. It~~ is scaled down to R = 20 m, u_{avg} = 7 m/s and λ_{opt} = 7. The resulting ~~, as such reaching~~ Reynolds numbers are closer to those of the wind tunnel tests, i.e. in ~~which are in~~ the range of $1.5 \cdot 10^6$ to $2 \cdot 10^6$ rather than $3 \cdot 10^6$ to $9 \cdot 10^6$.

(a) (b)

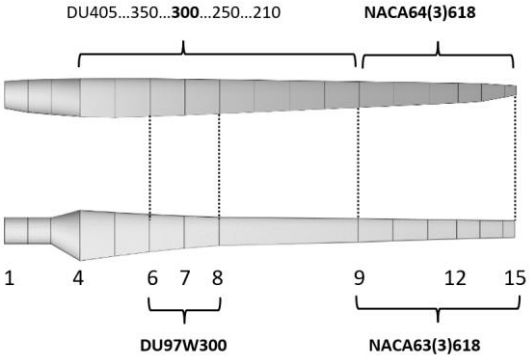

Formatted: Font: Italic

Formatted: Justified

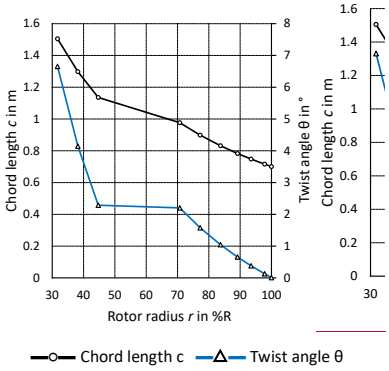

Figure 13. (a) Design of the generic rotor blade ~~based~~ based on ~~on~~ the NREL 5 MW reference wind turbine. (b) Geometry of the generic blade over the rotor radius.

Commented [D51]: RC1(Q20minor): the position of legend was fixed

Figure 13a ~~illustrates~~ shows that the DU97W300 is placed from blade position 6 to 8 and the NACA63(3)618 between position 9 ~~to~~ and 15. ~~The midspan region is~~ The midspan region, see position 8 to 9, ~~simply~~ interpolated between position 8 and 9 is simply interpolated for the purpose of this numerical part. Figure 13b shows the chord length $c(r)$ and the twist angle $\theta(r)$ ~~of the generic blade~~ at each blade position, ~~both of~~ which are determined by means of the ~~aerodynamic~~ blade optimization procedure of Schmitz (1956), as described by Gasch and Twele (2012),

$$c(r) = \frac{16\pi r}{B \cdot c_l(\alpha_{opt})} \sin^2\left[\frac{1}{3} tan^{-1}\left(\frac{R}{\lambda_{opt} \cdot r}\right)\right], \quad \lambda(r) = \frac{2\pi f r}{u_{stg}}, \qquad (15)\ (23)$$

where f is the rotational frequency in Hz and $\lambda(R) = \lambda_{opt}$.

$$\theta(r) = \varphi - \alpha_{opt} = \frac{2}{3}\tan^{-1}\left(\frac{R}{\lambda_{opt} \cdot r}\right) - \alpha_{opt}, \quad c(r) = \frac{16\pi}{B} \cdot \frac{r}{c_l(\alpha_{opt}(r))} \cdot \sin^2\left(\frac{1}{3} \cdot tan^{-1}\left(\frac{R}{\lambda_{opt} \cdot r}\right)\right), \qquad (16)\ (24)$$

$$\theta(r) = \varphi(r) - \alpha_{opt}(r) = \frac{2}{3} \cdot \tan^{-1}\left(\frac{R}{\lambda_{opt} \cdot r}\right) - \alpha_{opt}(r), \qquad (25)$$

Formatted Table

where B is the number of blades and φ ~~(r)~~ the inflow angle in °.

Commented [D52]: RC2: Paragraph was shortened.

The Schmitz design ~~, i.e. Eq. (24) and (25),~~ leads to elevated chord lengths and twist angles in the root region due to the decreasing rotational speed and thus λ (r)~~,~~ towards the blade root. For practical and logistical reasons, ~~the~~ c ~~(chord length in the root region, i.e.~~ r < 30 %R)~~,~~ is usually ~~reduced~~designed separately ~~in order~~ in order to ~~restrict~~ limit the volume and the weight of large rotor blades. Hence, the numerical results of the generic blade are only ~~considered to be~~ feasible between position 6 at r = 31.7 %R and the ~~very~~ tip. Besides, no specific tip design is implemented.

Next, two ~~generic~~ case studies are defined and presented based on Eq. (15~~15~~) and (16~~16~~)~~.~~ The first one ~~consists of~~is the retrofit application, i.e. ~~of~~ the PFC devices ~~that~~ are installed on ~~an~~ an existing rotor blade, for instance ~~during~~ regular

maintenance activities. The original blade design is based on ~~a~~ the smooth surface, i.e. the clean airfoil polars. Over time, ~~LER effects~~ LER occurs and the data files of the clean are replaced by the tripped baseline. ~~reduce~~ As a consequence, the aerodynamic efficiency and ~~thus~~ therefore the AEP is decreased. ~~Subsequently~~ During the third step, the polar data of both VGs and MGFs is imported ~~are installed~~ in order to recover some of the losses in power. ~~The simulation method is based on Hansen (2015). The BEM simulation entirely depends on the quality of the imported polar data. Apart from that, the results are interpolated between adjacent blade sections, see Figure 13a, b.~~ Furthermore, empirical correction algorithms are activated, ~~as described in Marten et al. (2013),~~ see Figure 14

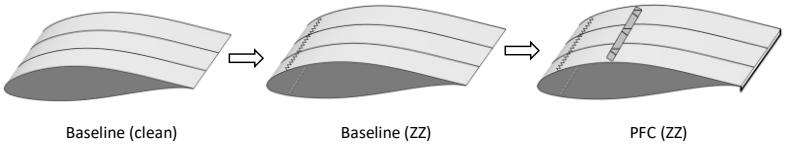

Figure 14. Retrofit application of passive flow control devices on a generic rotor blade section.

The second case study ~~consists is~~ ~~of~~ the ~~of~~ new design application. The ~~of~~ PFC devices ~~that~~ are installed as part of the blade manufacturing process on the ground. ~~The original, i.e. clean blade, is adversely affected by LER, as shown in Figure 21.~~ The performance of the clean and the tripped baseline blade, as previously depicted in Figure 14, is compared to an alternative ~~blade~~ configuration that includes ~~including t~~the PFC devices as part of the design process itself. Hence ~~itself~~, ~~see Figure 22,~~ the blade geometry, $c(r)$ and $\theta(r)$, is calculated separately for the alternative blade, PFC* (clean) and PFC* (ZZ), see Figure 15.

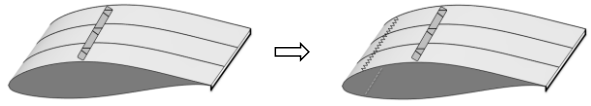

Figure 15. New design application of passive flow control devices on a generic rotor blade section.

~~The blade geometry, $c(r)$ and $\theta(r)$, is calculated separately for the clean baseline and the new blade including PFC devices. Applying Eq. (24) and for R, λ_{opt}, B to be identical, the ratio between the chord length at each blade position, r, is inversely proportional to the corresponding lift coefficients at the design AoA,~~

$$\frac{c(r)}{c_{PFC}(r)} = \frac{c_{l,PFC}(\alpha_{opt,PFC})}{c_l(\alpha_{opt})}, \quad (26)$$

~~According to Eq. (26), $c_{PFC}(r)$ decreases for larger $c_{l,PFC}$ values due to the MGF and VG effect, as illustrated in Figure 24.~~

5.3 Blade simulations

The rotor blade simulations are performed using the steady Blade Element Momentum (BEM) method based on Hansen (2015), which is embedded into QBlade, v99. ~~based on Hansen (2015). The BEM simulation~~ The BEM simulations entirely depend ~~entirely depends~~ on the quality of the imported polar data. ~~Apart from that, the results are interpolated between adjacent~~ at each blade section, see Figure 13a~~s~~, ~~.~~ Furthermore, empirical correction algorithms are activated, ~~as described in Marten et al. (2013),~~

Commented [D53]: RC2: Paragraph was shortened.
Formatted: Font: Not Italic
Formatted: Superscript
Formatted: English (United Kingdom)
Formatted: Superscript
Formatted: Justified
Formatted: Heading 2

including root and tip loss calculations~~es~~, thrust forces of heavily loaded rotors (Glauert correction) and spanwise crossflow effects, as described by Marten et al. (2013).~~ Apart from that, the results are interpolated between adjacent blade sections.~~ The power curves are determined with respect to ~~a~~ the rated power output of P_{max} = 600 kW at u_{rated} = 12 m/s. ~~In all cases, the~~ The basic pitch and rpm controller settings are optimized for reaching maximum power output. ~~Following Gasch and Twele (2012), the AEP or E is calculated by means of the Weibull distribution using the probability factors k = 2 for a typical site in central Europe and the average wind speed at hub height, u_{avg} = 7 m/s over an operational wind speed range between $u_{cut\text{-}in}$ = 3 m/s and $u_{cut\text{-}out}$ = 25 m/s.~~

Commented [D54]: RC2: the following sentences were removed

5.3.1 Retrofit application

The BEM ~~results~~ simulations of the retrofit application are presented. Figure 16 shows the AoA along the local rotor radius, r. The clean baseline coincides with $\alpha_{opt,clean}$ ~~(L/D_{max})~~ = 9.5° of the DU97W300 in the root, and $\alpha_{opt,clean}$ = 6.4° of the NACA63(3)618 in the tip region. Replacing the clean by the tripped polar data, the AoA are significantly increased, see Figure 16a. In fact, the ~~DU97W300 is stalling~~ root region is already stalling for ~~for~~ $\alpha > 10.5°$, so that the local L/D drops dramatically ~~towards the root region~~, see Figure 16b. This adverse effect of forced LE transition ~~of the ZZ tape~~ is partly compensated for by the PFC devices. Hence, ~~the~~ the AoA are ~~much~~ closer to $\alpha_{opt,clean}$, ~~so that~~ and the $L/D(r)$ is partly recovered, ~~indicating that the PFC configuration is less sensitive to LER.~~ Figure 16c shows the power coefficients over the complete operational range of the rotor. In the tripped case, the ~~c_p~~ power curve is shifted towards higher TSR, ~~so that~~ leading to $\lambda(c_{p,max,ZZ}) = 8$ rather than $\lambda_{opt} = 7$. ~~Hence~~ As a result, $c_{p,max,clean}(\lambda_{opt}) = 0.48$ is decreased by 13 % to $c_{p,max,ZZ}(\lambda_{opt}) = 0.42$. After the retrofit application, the c_p curve is closer to the design point with $c_{p,max,PFC}$ ~~(ZZ)~~ (λ_{opt}) = 0.45, and the drop ratio between clean and tripped is decreased by 57 % ~~Edamame AEP annual E_{clean} = 152 MWh, E_{ZZ} = 146 MWh (-4 %) and E_{PFC} = 152 MWh (-4 %) the significant energy yield loss of roof Emin~~ is approximately halved by the retrofit application of MGFs and VGs.

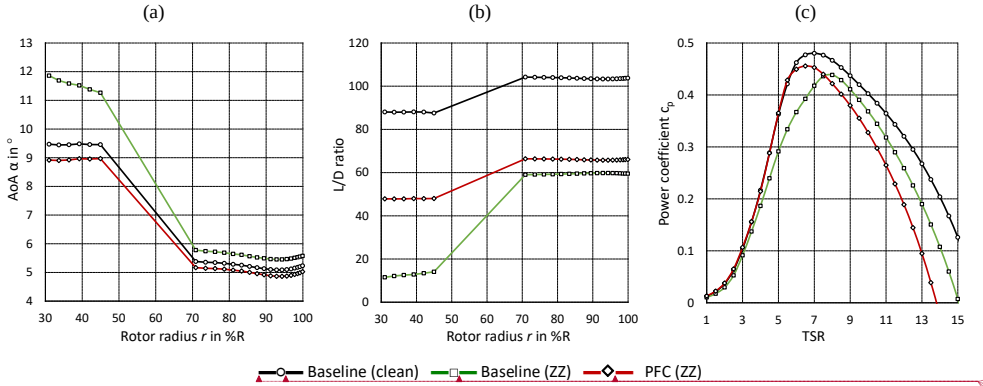

Figure 16. Rotor blade performance simulation of baseline and retrofit application. (a) AoA over rotor radius at λ_{opt} = 7. (b) L/D over rotor radius at λ_{opt} = 7. (c) Power coefficients over TSR.

Formatted: Font: Italic

Formatted: English (United States)

Formatted: English (United States)

Formatted: English (United States)

Formatted: English (United States)

~~Enhanced APD parameter E_{ap} = 150 MWh, E_{ap} = 146 MWh (98 %) and E_{apg} = 150 MWh (41 %) bigger as already known due to fixed LP and improved blade design for MC and VG.~~

The BEM results of the new design application are presented. According to Eq. (15~~15)~~, the lift increase caused by the MGFs, see Figure 17a, leads to a significant chord length reduction, ~~as illustrated in Figure 24a and b~~. Comparing the baseline cases, the optimum chord length is reduced by 23.4 % in the root and by 12 % in the tip region, as illustrated in Figure 17b. Regardless of the structural-dynamic considerations, this approach might contribute to the development of more slender blades and thus saving material costs, as previously suggested by Fuglsang et al. (2004), see Sect. 1.5. Moreover, periodic gravitational load alternations as well as fatigue loads are potentially mitigated by reducing the blade weight.

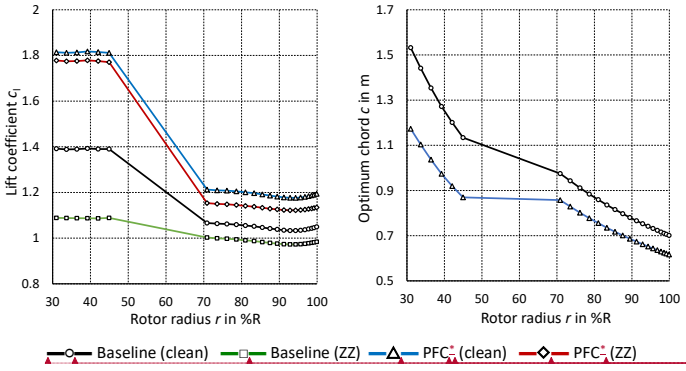

Figure 17. Blade geometry of baseline and new design application at λ_{opt} = 7. (a) Lift coefficients over rotor radius (b) Optimum chord length over rotor radius.

~~Compared to the baseline case, $c_{PFC}(r)$ is reduced by 23.4 % in the root and by 12 % in the tip region. Regardless of any structural-dynamic considerations, this approach potentially contributes to the development of more slender and thus lighter blades. Apart from saving material costs, as previously suggested by Fuglsang et al. (2004), see Sect. 1.5, periodic gravitational load alternations and thus fatigue loads might be mitigated.~~

Next, Figure 18 shows the BEM simulation ~~results~~of the new design application. It is noted that ~~It is reiterated that t~~the clean and tripped baseline ~~configurations~~ curves, Baseline (clean) and Baseline (ZZ), are identical to previous ~~are identical to the retrofit application~~Figure 16. First of all, PFC* (clean) and PFC* (ZZ) lead to similarly high design AoA, $\alpha_{opt,PFC} \approx 12°$ towards the root, see Figure 18a. Apart from that, stall is delayed by the VGs until approximately 16°, which is not shown here. In the tip region, the MGF only leads to a marginal increase regarding α (λ_{opt}). Figure 18b illustrates that, in the clean case, the

Formatted Table
Formatted: English (United States)
Formatted: English (United States)
Formatted: English (United States)
Formatted: English (United States)
Formatted: Superscript
Formatted: English (United States)
Formatted: English (United States)
Formatted: English (United States)
Formatted: Font: Not Italic
Formatted: Font: Not Italic
Formatted: Font: Not Italic

aerodynamic efficiency is decreased towards the root region due to the drag penalty of the PFC devices, whereas the MGF achieves a slight *L/D* improvement towards the tip. In contrast to that, the PFC* (ZZ) improves the aerodynamic efficiency significantly throughout the complete blade length, as compared to Baseline (ZZ). Hence, the PFC* configuration appears to be less sensitive to forced LE transition. Next, Figure 18c shows the corresponding power curves. In both PFC* (clean) and PFC* (ZZ), $c_{p,max}$ remains at $\lambda_{opt} = 7$. As a consequence, $c_{p,max} = 0.48$ is almost identical compared to Baseline (clean), despite moderate differences at elevated TSR for $\lambda > \lambda_{opt}$. In the tripped cases, $c_{p,max}(\lambda_{opt}) = 0.45$ is reduced by only 4.6 % relating PFC (ZZ) to PFC (clean) rather than by 13 % with regards to the baseline cases. Again, the power loss due to forced LE transition is at least halved and the rotor blades are significantly more slender due to the new design application of MGFs and VGs.

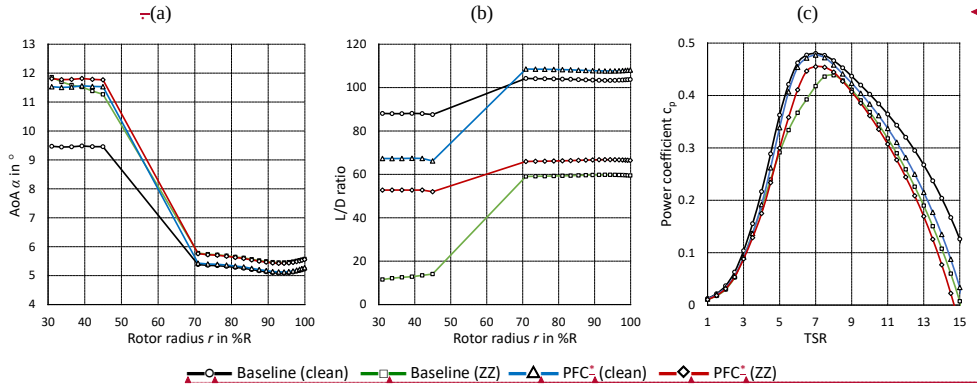

Figure 18. Rotor blade performance simulation of baseline and new design application. (a) AoA over rotor radius at $\lambda_{opt} = 7$. (b) L/D over rotor radius at $\lambda_{opt} = 7$. (c) Power coefficients over TSR.

Looking at the root region, the design AoA at $\lambda_{opt} = 7$ is shifted from $\alpha_{opt,Base(clean)} \approx 9.5°$ to $\alpha_{opt,Base(ZZ)} \approx 11.5°$, where the DU97W300 is already stalling, see Figure 25a. The clean and the tripped PFC cases, on the other hand, lead to a significantly higher design AoA, i.e. $\alpha_{opt,PFC} \approx 12°$. Unlike the baseline configurations, stall is delayed by the VGs until $\alpha_{cl,max,PFC} \approx 16°$. In the tip region, the MGF configuration leads to identical $\alpha(\lambda_{opt})$ compared to the respective baseline. As a result, $L/D_{clean}(r)$ in the root region is decreased compared to the clean baseline due to the drag penalty of the PFC devices, see Figure 25b. However, in the tripped case, the *reduction of* $L/D_{PFC(ZZ)}(r)$ is significantly less severe compared to the baseline case because of stall delay. Moreover, looking at the tip region, the MGF effect leads to elevated $L/D(r)$ in both the clean and, particularly, the tripped case. Again, the L/D curves indicate that the PFC configuration is less sensitive to LER. Figure 25c shows the c_p curves. In the tripped baseline case, the design TSR is shifted to $\lambda(c_{p,max,ZZ}) = 8$ rather than $\lambda_{opt} = 7$. For both PFC cases, $c_{p,max,PFC}$ remains at $\lambda_{opt} = 7$, so that the overall shape of the clean baseline curve is maintained. As a consequence, $c_{p,max,PFC(clean)} = 0.48$ is almost identical to the clean baseline, despite moderate differences at elevated TSR, i.e. for $\lambda > \lambda_{opt}$. Furthermore, $c_{p,max,PFC(ZZ)}(\lambda_{opt}) = 0.45$ decreases by only 4.6 % rather than 13 % compared to the respective clean case. The AEP amounts to $E_{Base(clean)} = 1594$ MWh and $E_{Base(ZZ)} = 1464$ MWh (8.2%), compared to $E_{PFC(clean)} = 1587$ MWh and $E_{PFC(ZZ)} = 1536$ MWh (3.6%). Hence, the difference between the clean baseline and clean PFC configuration is minor. In addition, the blades are more slender and the energy decline due to forced LE transition is mitigated by the new design application of MGFs and VGs.

Formatted Table
Formatted: English (United States)
Formatted: English (United States)
Formatted: English (United States)
Formatted: English (United States)
Formatted: English (United States)
Formatted: English (United States)
Formatted: English (United States)
Formatted: Subscript
Formatted: Font: Italic
Formatted: Font: Italic
Formatted: Font: Italic
Formatted: Font: Not Italic

6 Conclusions

Commented [D55]: RC2: The conclusions were revised.

~~The present study investigates the use of mini Gurney flaps and their combination with vortex generators for improved rotor blade performance of horizontal axis wind turbines. The main conclusions are summarized alongside the main sections of this report.~~

For that, wind tunnel tests are conducted using the NACA63(3)618 and the DU97W300. Lift and drag are measured by means of a force balance and a wake rake, respectively. The baseline results are successfully validated against literature data. The impact of MGFs and VGs on the polar curves depends on whether transition is free or fixed on the airfoils. The configurations with just the MGFs increase the lift performance under pre-stall conditions. Furthermore, the aerodynamic efficiency is maintained in the clean, and improved in the tripped case. Looking at the combined configurations, the VG effect is superposed by the MGF effect, leading to both stall delay and the pre-stall lift increase. In the clean case, the aerodynamic efficiency is decreased due to the combined drag penalty, whereas in the tripped case, it is significantly improved. Furthermore, VGs coupled with MGFs are preferred over the VG (only) configuration due to the additional pre-stall lift increase.

The experimental polar data is imported into the software QBlade in order to design and to simulate a generic rotor blade. The NACA63(3)618 is equipped with the smallest MGF height of 0.25%c in the tip region. The medium size MGF of 0.5 %c and the VG height of 1.1 %c are both attached to the DU97W300 in the root region. The BEM simulations are based on two case studies, the retrofit application on an existing, and the new design application on an alternative blade configuration. The retrofit application alleviates the adverse effects of forced leading edge transition. Separation is delayed in the root region and the aerodynamic efficiency and thus power output is recovered towards the tip region. The new design application leads to a more slender blade while maintaining the rotor power. Again, the alternative blade appears to be more resistant against leading edge roughness effects.

Further research on MGFs and their interaction with VGs is recommended, especially considering leading edge roughness effects and erosion. Next steps involve the design of sub boundary layer VGs in conjunction with MGFs to further reduce the drag penalty. Moreover, a complete aeroelastic simulation is required, especially regarding open field tests of MGFs in combination with VGs on large wind turbine rotor blades.

Appendix A: Wind tunnel corrections

Commented [D57]: RC2: All Appendices were reorganized

Formatted: Heading 1

Following from the experimental setup, see Sect. 3.2, the calculation of the wind tunnel wall effects on the uncorrected lift and drag polars, $c_{l,raw}(\alpha)$ and $c_{d,raw}(\alpha)$, is summarized. According to Barlow et al. (1999), the wind tunnel blockage, ε, is the sum of the solid and the wake blockage factors,

$$\varepsilon = \varepsilon_{solid} + \varepsilon_{wake} = \Lambda\mu + \frac{c}{4h_{wt}} c_{d,raw}, \quad (17)$$

where Λ refers to the so-called body shape factor, which is a function of the maximum airfoil thickness and h_{wt} is the height of the wind tunnel. For clarity, $\mu = \frac{\pi^2}{48}\left(\frac{c}{h_{wt}}\right)^2$ is introduced as an auxiliary constant.

Based on Eq. (17~~17~~), the solid and the wake blockage correction is applied on the following parameters at each static AoA,

$$c_d = c_{d,raw}(1 - 3\varepsilon_{solid} - 2\varepsilon_{wake}), \quad (18)$$

$$c_l = c_{l,raw}(1 - \mu - 2\varepsilon), \quad (19)$$

$$Re = Re_{raw}(1 + \varepsilon), \quad (20)$$

$$\alpha = \alpha_{raw} + \frac{57.3\mu}{2\pi}\left(c_{l,raw} + 4c_{m,raw}\right), \quad (21)$$

$$c_m = c_{m,raw}(1 - 2\varepsilon) + 0.25\mu c_l, \quad (22)$$

where c_m refers to the moment coefficient at 0.25c.

Eq. (18~~18~~) to (22~~22~~) are embedded into the data post-processing script.

Appendix ~~A~~B: ~~AH93W174~~NACA63(3)618

~~4.1.3~~B1. Vortex generators plus ~~Mini~~ Gurney flaps

Figure 19~~Figure 19~~ ~~illustrates~~shows ~~-~~the polar curves of ~~all~~the VG + GF configurations based on the NACA63(3)618. As ~~previously~~ presented in Sect. 4.2.1, ~~,~~the VG is superposed by the GF effect, leading to both stall delay and pre-stall lift increase. Compared to the corresponding VG (only) configurations, *L/D (a)* is maintained in the clean, and slightly improved in the tripped cases. For clarity, characteristic lift and L/D values are summarized in Table 9~~Table 9~~.~~Looking at the VG (only) cases, stall is delayed by around 2°, coupled with a substantial increase in $c_{l,max}$; see Figure 14a. Furthermore, VGs lead to a more abrupt stall behaviour and thus adverse load excursions, as previously reported by Mueller-Vahl et al. (2012). In all combined cases, the GF is added to the VG effect as a constant lift and drag increase. For clarity, characteristic lift and *L/D* values are summarized in Table 6.~~

(a) (b)

Formatted: Font color: Auto

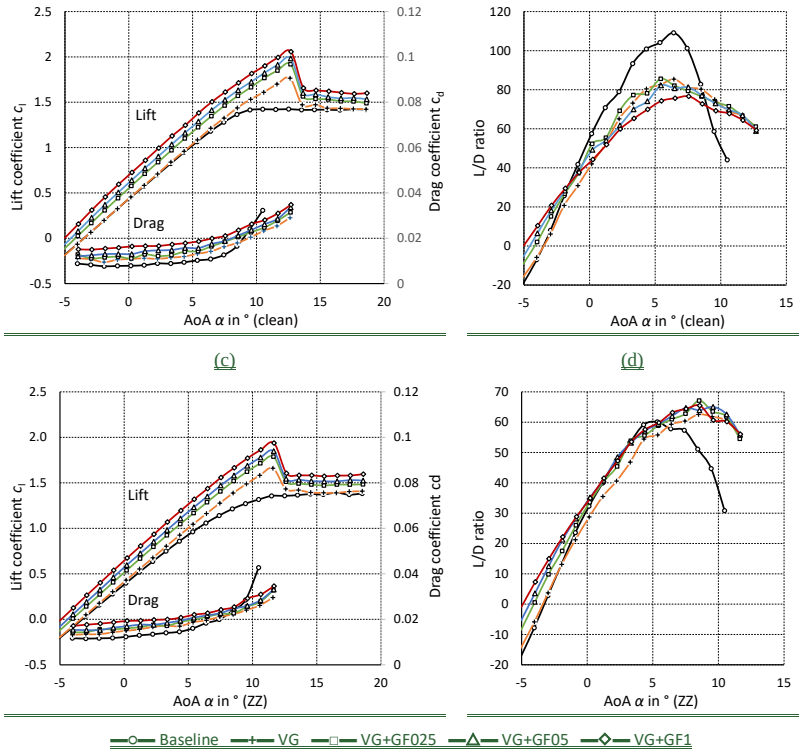

Figure 19. NACA63(3)618. Vortex generators and Gurney flaps. (a) Lift and drag coefficients (clean). (b) L/D ratio (clean). (c) Lift and drag coefficients (ZZ). (d) L/D ratio (ZZ).

Table 9. NACA63(3)618. Vortex generators plus Gurney flaps. Characteristic values.

	Clean		~~Tripped~~ZZ	
	$c_{l,max}$ (α)	L/D_{max} (α)	$c_{l,max}$ (α)	L/D_{max} (α)
Baseline	1.42 (10.5°)	109 (6.4°)	1.32 (10.5°)	60 (5.4°)
VG	1.76 (12.7°)	85 (6.4°)	1.66 (11.6°)	63 (8.5°)
VG+GF025	1.92 (12.7°)	82 (6.4°)	1.79 (11.6°)	67 (8.5°)
VG+GF05	1.98 (12.7°)	81 (6.4°)	1.85 (11.6°)	64 (8.5°)
VG+GF1	2.06 (12.7°)	76 (6.4°)	1.94 (11.6°)	65 (8.5°)

~~According to Figure 14a and c, drag is reduced at elevated AoA due to the effect of stall delay. However, in the clean case, the drag penalty at low and moderate AoA causes $L/D_{max,clean}$ to decrease. Hence, the preferred results are achieved for VG + GF025 compared to the remaining configurations, see Figure 14b. Under tripped conditions, all PFC devices are capable of maintaining L/D at low and moderate AoA. Moreover, $L/D_{max,ZZ}$ increases significantly, as it is shifted by around 2° and thus recovering a wide area of otherwise separated flow in the range of $6.5° < \alpha < 11.6°$, see Figure 14d. Again, VG + GF025 is the preferred configuration. Overall, the polar graphs indicate that the VG is superposed by the GF effect. In fact, looking at both the lift and the L/D curves of Figure 14 and Figure 28, the combined cases prove to be beneficial compared to the VG (only) configurations. The reason for this phenomenon is suspected to be the beneficial wake flow interaction between both PFC devices, as previously illustrated in and further discussed in the following section.~~

B2. Rectangular versus triangular Gurney flaps

Formatted: Heading 2

Timmer and van Rooij (2003) ~~and~~as well as Fuglsang et al. (2003) reported that rectangular and triangular GFs of identical height generate very similar aerodynamic effects~~no significant changes comparing the effect of rectangular and triangular GFs of identical height~~, apart from minor differences in drag~~, apart from minor differences in drag~~. In order to verify this observation, the NACA63(3)618 is equipped with ~~both GF profiles, as previously illustrated in a: thin~~ angle sections made of brass versus isosceles triangles made of ~~a standard~~ thermoplastic material, see Figure 1a.~~,~~ In Figure 20~~Figure 20~~, t~~Figure 10 compares t~~he lift ~~over drag~~ over the drag coefficients are compared in both the clean and the tripped cases looking at each GF configuration separately. It is noted that the smallest triangular size, $h_{MGF,\Delta} = 0.33$ %c is larger than the corresponding rectangular profile, $h_{MGF,L} = 0.25$ %c~~, see Figure 10a.~~ ~~Overall~~In all cases, ~~, all~~the triangular or wedge shaped profiles show~~s~~ a slight decrease in both lift and drag, ~~which is visible in terms of~~see Figure 20~~Figure 20~~b and c~~, GF05 and GF1, see Figure 10b and c.~~ ~~Nonetheless~~Apart from that, the effect on the airfoil polars is very similar between both GF profiles.~~the agreement between the two profiles is considered satisfying. In the remainder of this report, all GF configurations refer to the rectangular, or L-shaped, profile.~~

(a) (b) (c)

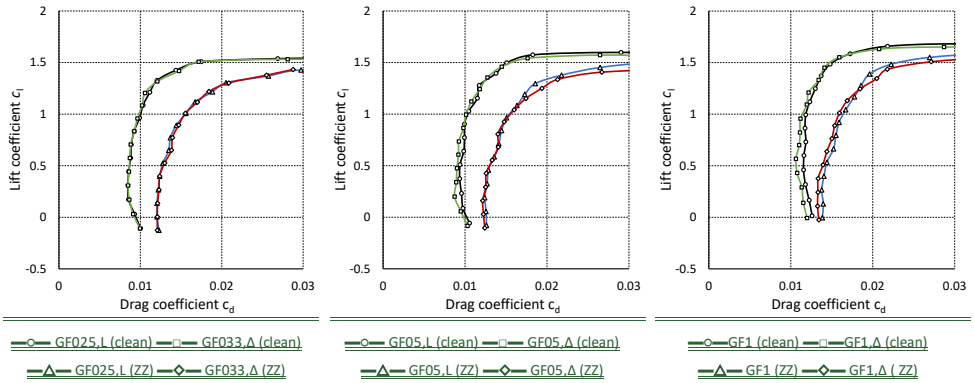

Figure 20. NACA63(3)618. Rectangular (L) versus triangular (Δ) Gurney flap profiles. Lift over drag curves in clean and tripped cases (a) $h_{MGF,L}$ = 0.25 %c and $h_{MGF,\Delta}$ = 0.33 %c. (b) h_{MGF} = 0.5 %c. (c) h_{GF} = 1 %c.

~~The wind tunnel results of the AH93W174 are presented alongside the NACA63(3)618 and the DU97W300, see Sect. 4. For brevity, only the L/D graphs and the characteristic lift and L/D values are included in A2 and A3.~~

~~A1. Baseline~~

~~Figure 26 shows the clean and the tripped polar curves. Stall is initiated at $\alpha_{cl,max}$ = 10.5° and $\alpha_{opt,clean}$ = 8.5° decreases to $\alpha_{opt,ZZ}$ = 5.3°, see Figure 26a. Figure 26b shows that the aerodynamic efficiency drops from $L/D_{max,clean}$ =118 to $L/D_{max,ZZ}$ = 61. For clarity, characteristic lift and L/D values are summarized in Table 11.~~

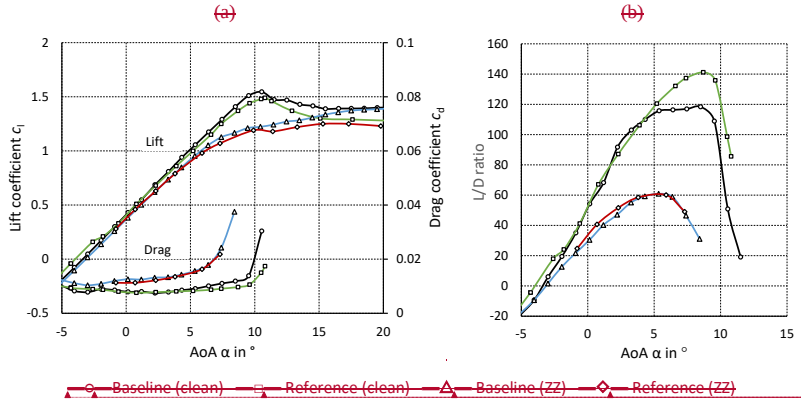

Formatted: English (United Kingdom)
Formatted: Normal
Formatted: English (United States)
Formatted: English (United States)
Formatted: English (United States)
Formatted: English (United States)
Formatted: English (United States)

~~Figure 26. AH93W174. Clean and tripped baseline cases at $Re = 1.5 \cdot 10^6$ compared to reference data from Althaus (1996) at $Re = 1.5 \cdot 10^6$. (a) Lift and drag coefficients. (b) L/D ratio.~~

~~Figure 27. AH93W174. Gurney flaps. (a) L/D ratio (clean). (b) L/D ratio (ZZ).~~

~~**A3. Vortex generators plus Mini Gurney flaps**~~

~~Figure 28. AH93W174. Vortex generators and Gurney flaps. (a) L/D ratio (clean). (b) L/D ratio (ZZ).~~

Appendix C: DU97W300

C1. Data validation

Commented [D58]: RC2: The validation of the measurement results were restricted to one airfoil. The results of the NACA validation was deleted.

The baseline and the VG measurements of the DU97W300 are compared to reference data in order to validate the experimental setup. Baldacchino et al. (2018) performed similar experiments in the low turbulence wind tunnel of the DU. The airfoil chord length was $c = 0.65$ m (here 0.6 m) and $Re = 2 \cdot 10^6$ (here: $Re = 1.5 \cdot 10^6$) with a free stream turbulence intensity of below 0.1% (here: 0.3 %). Lift was determined from surface pressure measurements and drag by means of a wake rake, which was positioned at a distance of 60 %c (here 100%c) away from the airfoil TE. Forced LE transition was triggered by means of ZZ tape with $h_{ZZ} = 0.17$ mm at $x_{ZZ} = 5.0$ %c on the suction side, as opposed to the more aggressive tripping of the current setup with $h_{ZZ} = 0.3$ mm on both the suction and the pressure side. The VG configurations included $h_{VG} = 0.77$ %c and $D = 7h_{VG}$ at $x_{VG} = 30$%c, as compared to the current setup with $h_{VG} = 1.1$ %c. Figure 21~~21~~ shows the direct comparison between the polar data. For clarity, characteristic lift and L/D values are summarized in Table 10~~10~~.

Figure 21~~21~~a and c show very good agreement between the lift curves of both the baseline and the VG configurations. However, the stall behaviour is smoother looking at the current measurements. In the clean case, drag is elevated compared to the reference data leading to slightly decreased L/D (α) curves. The main reasons are the differences in the Reynolds number and the inflow turbulence intensity. Furthermore, due to the larger VG height, drag is slightly higher in the pre-stall region, as compared to the DU measurements. In the tripped case, the more pronounced differences in both c_d (α) and thus L/D (α) are due to the more aggressive tripping of the current setup. Overall, the results are in very good agreement with the reference data, as highlighted in Table 10~~10~~.

Table 10. DU97W300. Characteristic values. Reference data is adopted from Baldacchino et. al (2018)

	Clean		**ZZ**	
	$c_{l,max}$ (α)	L/D_{max} (α)	$c_{l,max}$ (α)	L/D_{max} (α)
Baseline	1.64 (12.6°)	88 (9.5°)	1.13 (11.4°)	41 (7.4°)
Baseline (reference)	1.53 (12.4°)	90 (9.3°)	1.11 (9.2°)	50 (6.2°)

Formatted: Font: Not Bold

VG	1.91 (15.6°)	71 (12.6°)	1.82 (14.6°)	52 (12.6°)
VG (reference)	1.94 (15.5°)	73 (11.3°)	1.86 (15.4°)	59 (13.4°)

745

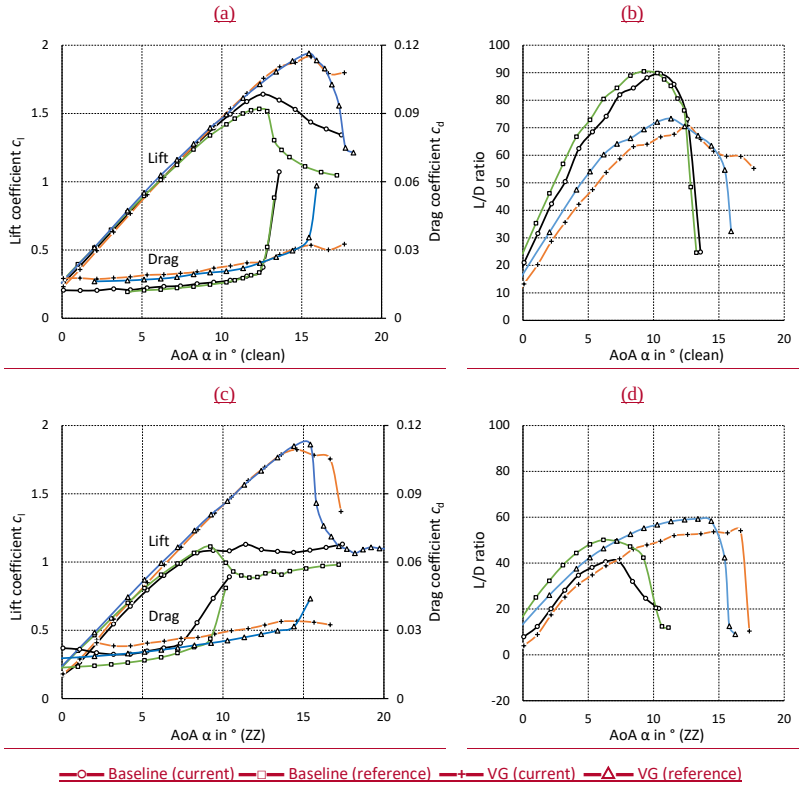

Figure 21. DU97W300. Clean and tripped cases. Baseline and VG configurations at $Re = 1.5 \cdot 10^6$ compared to reference data from Baldacchino et al. (2018) at Re = $2 \cdot 10^6$. (a) Lift and drag coefficients. (b) Lift to drag ratio.

C2. Gurney flaps

Figure 22~~22~~ shows the polar curves of the GF configurations based on the DU97W300. As presented in Sect. 4.1.1, the increase in both lift and drag depends on the GF height and the shape of the polar curves is basically maintained. Furthermore, the beneficial GF effect on the aerodynamic efficiency is more pronounced in the tripped case. Figure 22~~22~~b shows that, in the clean case, L/D (α) is maintained applying either of the MGFs, whereas it is decreased using the GF1. According to Figure 22d, the performance deterioration due to forced LE transition is alleviated by all GFs, with GF05 achieving the preferred results in terms of $L/D_{ZZ}(\alpha)$. For clarity, characteristic lift and L/D values are summarized in Table 11~~11~~.

Formatted Table

Formatted: Heading 2

Formatted: Font: Not Italic

Formatted: Font: Italic

Formatted: Font: Italic

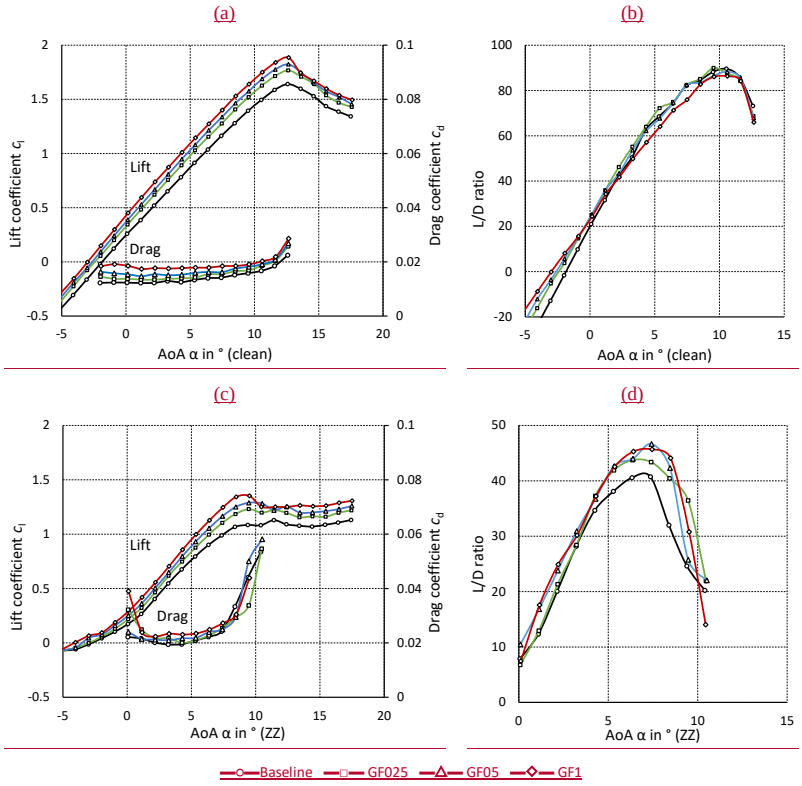

Figure 22. DU97W300. Gurney flaps. (a) Lift and drag coefficients (clean). (b) L/D ratio (clean). (c) Lift and drag coefficients (ZZ). (d) L/D ratio (ZZ).

Table 11. DU97W300. Gurney flaps. Characteristic values.

	Clean		**ZZ**	
	$c_{l,max}$ (12.6°)	L/D_{max} (9.5°)	$c_{l,max}$ (10.4°)	L/D_{max} (7.4°)
Baseline	1.64	88	1.08	41
GF025	1.77	90	1.20	43
GF05	1.82	87	1.28	47
GF1	1.89	86	1.25	46

Data availability.

Measurement data and results can be provided by contacting the corresponding author.

Author contribution

Johannes Fischer designed and fabricated the wake rake and the vortex generators. Jörg Alber validated the wake rake measurements and designed the Gurney flaps. Jörg Alber, Marinos Manolesos, Guido Weinzierl-Dlugosch, Johannes Fischer and Alexander Schönmeier prepared and conducted the wind tunnel experiments. Jörg Alber performed the airfoil and rotor blade simulations. Jörg Alber and Alexander Schönmeier processed the experimental and numerical data. Jörg Alber wrote the manuscript ~~with the support of all co-authors,~~ and managed the review process~~who contributed with important suggestions,~~ with the support of all co-authors.~~.~~

Competing interests

The authors declare that they have no conflict of interest.

Acknowledgements

The authors would also like to appreciate the constant support of the technicians of the Hermann-Föttinger Institut at the Technische Universität Berlin.

References

Abbott, I.H., and von Doenhoff, A.E.: Theory of Wing Sections, Dover publications, Inc. New York, ISBN 100486605868, 1959.

Use on Wind Turbine Blades, in: Proceedings of the ASME Turbo Expo 2017, Volume 9, Wind Energy, Charlotte, North Carolina, USA, Paper GT2017-64475, https://doi.org/10.1115/GT2017-64475, June, 2017.

a wind turbine, Journal of Physics: Conference Series, Volume 524, http://dx.doi.org/10.1088/1742-6596/524/1/012082, 2014.

relative thickness equipped with vortex generators, Journal of Physics: Conference Series, Volume 1037, Issue 2, http://dx.doi.org/10.1088/1742-6596/1037/2/022044, 2018.

Formatted: Indent: Left: 1.27 cm

Field Code Changed

Field Code Changed

generators mounted on the entire blade, Journal of Physics: Conference Series, Volume 753, Issue 2, http://dx.doi.org/10.1088/1742-6596/753/2/022001, 2016.

MW Reference Wind Turbine, Technical University of Denmark, DTU Wind Energy Report-I-0092, June 2013.

passive vortex generators on a 30% thick airfoil, Wind Energy. 2018, Vol. 21, p. 745-765, https://doi.org/10.1002/we.2191, 2018.

Aerospace Sciences, Vol. 46, Issue 1, p. 1-27, ISSN 0376-0421, https://doi.org/10.1016/j.paerosci.2009.08.002, 2010.

Barlow, J. B., Rae, W. H. and Pope, A.: Low-Speed Wind Tunnel Testing, John Wiley & Sons, 3rd edition, USA, https://doi.org/10.2514/2.633, 1999.

Fluids 2000 Conference and Exhibit, Denver, USA, Paper 2000-2315, https://doi.org/10.2514/6.2000-2315, June 2000.

Number: 01250001.3, Date of Patent: 2nd of January 2001.

September, 1985.

Patent: 7th of May 2002.

Cole, J. A., Vieira, B. A. O., Coder, J. G., Premi, A. and Maughmer, M. D.: Experimental Investigation into the Effect of Gurney Flaps on Various Airfoils, Journal of Aircraft, Vol. 50, No. 4, https://doi.org/10.2514/1.C032203, 2013.

Number Aerodynamics, Vol. 54, Springer Berlin, Heidelberg, https://doi.org/10.1007/978-3-642-84010-4_1, 1989.

ASME. J. Sol. Energy Eng, Vol. 126, p. 1002-1010, https://doi.org/10.1115/1.1766024, November 2004.

Risoe-R-1375(EN), 2003.

Heidelberg, https://doi.org/10.1007/978-3-642-22938-1, 2012.

Aerodynamics Conference, San Diego, USA, Paper 1995-1881-CP, https://doi.org/10.2514/6.1995-1881, June, 1995.

Field Code Changed

Field Code Changed

Field Code Changed

Formatted: English (United States)

Formatted: English (United States)

Formatted: Indent: First line: 1.27 cm

Formatted: German (Germany)

Formatted: Indent: First line: 1.27 cm

Field Code Changed

Formatted: German (Germany)

Formatted: German (Germany)

with Passive Flow Control Technologies, p. 11-16, in: Stoevesandt B., Schepers G., Fuglsang P., and Yuping S. (eds): Handbook of Wind Energy Aerodynamics, Springer, Cham., https://doi.org/10.1007/978-3-030-05455-7_6-1, 2020.

Committee for Aeronautics, N.A.C.A. Technical Memorandum, No. 714, Washington, 1933.

UK, https://doi.org/10.4324/9781315769981, 2015.

22th of August 1989.

Aircraft, Vol. 37, No. 2, https://doi.org/10.2514/2.2593, April 2000.

Development, National Renewable Energy Lab. (NREL), Technical Report NREL/TP-500-38060, https://doi.org/10.2172/947422, 2009.

Blades, Wind Engineering, https://www.jstor.org/stable/43749607,1996.

9, Paper 76-406, San Diego, USA, https://doi.org/10.2514/3.58406, 1978.

Sciences, Vol. 38, Issues 4–5, p. 389-420, ISSN 0376-0421, https://doi.org/10.1016/S0376-0421(02)00010-6, 2002.

Mechanical Engineering Science, Vol. 227, Issue 12, p. 2701-2706, https://doi.org/10.1177/0954406213478533, 2013.

on Wind Turbine Performance, Journal of Physics: Conference Series, Vol. 1618, http://dx.doi.org/10.1088/1742-6596/1618/5/052082, 2020.

experiencing three-dimensional separation, Journal of Wind Engineering and Industrial Aerodynamics, Vol. 142, p.130-148, ISSN 0167-6105, https://doi.org/10.1016/j.jweia.2015.03.020, 2015.

Simulation Tool for Vertical and Horizontal Axis Wind Turbines, ASME Turbo Expo 2013, Volume 8, San Antonio, Texas, USA, Paper GT2013- 94979, https://doi.org/10.1115/GT2013-94979, June 2013.

Berlin, DOI:10.14279/depositonce-10646, https://depositonce.tu-berlin.de/handle/11303/11758, 2020.

Formatted: Indent: Left: 1.27 cm

Field Code Changed

Formatted: English (United States)

Formatted: Indent: Left: 1.27 cm

Field Code Changed

Modifications, Journal of Aircraft, Vol. 43, No. 1, https://doi.org/10.2514/1.14294, February 2006.

Strömungsablösungen, PhD Thesis, Technische Universität Berlin, Hermann-Föttinger-Institut für Strömungsmechanik, ~~December~~ 2000.

combined Wind Tunnel and Wind Turbine Parametric Study, ASME Turbo Expo, GT2012-69197, https://doi.org/10.1115/GT2012-69197, 2012.

Edge Serrations, AIAA Journal, Vol. 47, No. 6, https://arc.aiaa.org/doi/10.2514/1.38888, June 2009.

energy production and performance of a Multi-MW wind turbine, in: Renewable Energy, Vol.165, p. 701-715, https://doi.org/10.1016/j.renene.2020.11.071, 2021.

Berlin, Fakultät V - Verkehrs- und Maschinensysteme, 2013.

https://www.cfd.tu-berlin.de/research/flowcontrol/gurneys_en/ (last access: 17 October 2020), 2004a.

Control Conference Portland, Oregon, USA, Paper 2004-2417, https://doi.org/10.2514/6.2004-2417, June 2004b.

https://doi.org/10.1007/978-3-662-52919-5, 2000.

performance), Wiss. Zeitschrift der Universität Rostock, 5. Jahrgang, 1955/56.

Aerospace Sciences Meeting, Journal of Aircraft, Vol. 31, No. 3, Paper 93-0647, Reno, Nevada, USA, https://doi.org/10.2514/3.46528, May, 1994.

Sol. Energy Eng, Vol. 125(4), p. 488-496, https://doi.org/10.1115/1.1626129, November 2003.

blades, 47th AIAA Aerospace Sciences Meeting, Orlando, Florida, AIAA 2009-268, https://doi.org/10.2514/6.2009-268, January 2009.

97-W-300Mod, Wind Energ., 7: 295-307, https://doi.org/10.1002/we.136, 2004.

Field Code Changed
Field Code Changed
Formatted: Indent: First line: 1.27 cm
Formatted: English (United States)
Field Code Changed
Formatted: German (Germany)
Formatted: German (Germany)
Formatted: Indent: First line: 1.27 cm
Field Code Changed
Field Code Changed
Formatted: English (United States)
Formatted: English (United States)
Formatted: English (United States)
Formatted: Indent: Left: 1.27 cm
Field Code Changed
Formatted: English (United States)
Formatted: German (Germany)
Formatted: Indent: First line: 1.27 cm
Field Code Changed
Formatted: German (Germany)
Formatted: German (Germany)

Aerospace Science Meeting and Exhibit, Reno, Nevada, USA, AIAA Paper 2003-0350, January 2003, https://doi.org/10.2514/6.2003-350.

https://nozebra.ipapercms.dk/Vestas/Communication/Productbrochure/ProductImprovements/aerodynamic-upgrades-case-study/, ~~(last access: 17th of October 2021),~~ 2019 (last access: 17th of March 2022).~~.~~

Sciences, Vol. 44, Issue 1, p. 22-47, ISSN 0376-0421, https://doi.org/10.1016/j.paerosci.2007.10.001, January 2008.

Wilcox, B. J., White, E. B., and Maniaci, D. C.: Roughness Sensitivity Comparisons of Wind Turbine Blade Sections, Sandia Report, SAND2017-11288, https://doi.org/10.2172/1404826, 2017.

January 1935.

Formatted: English (United States)

Field Code Changed

Formatted: English (United States)

Formatted: Indent: Left: 1.27 cm

Field Code Changed